

High Latitude Ionospheric Electrodynamics During STEVE and Non-STEVE Substorm Events

Valerie Claire Svaldi¹, Tomoko Matsuo², Liam Kilcommons³, and Bea Gallardo-Lacourt⁴

¹Mechanical Engineering Department, Colorado School of Mines

²Ann and H.J. Smead Department of Aerospace Engineering Sciences, University of Colorado Boulder

³University of Colorado Boulder

⁴NASA GSFC

November 21, 2022

Abstract

Previous studies have shown that Strong Thermal Emission Velocity Enhancement (STEVE) events occur at the end of a prolonged substorm expansion phase. However, the connection between STEVE occurrence and substorms and the global high-latitude ionospheric electrodynamics associated with the development of STEVE and non-STEVE substorms are not yet well understood. The focus of this paper is to identify electrodynamics features that are unique to STEVE events through a comprehensive analysis of ionospheric convection patterns estimated from SuperDARN plasma drift and ground-based magnetometer data using the Assimilative Mapping of Geospace Observations (AMGeO) procedure. Results from AMGeO are further analyzed using principal component analysis and superposed epoch analysis for 32 STEVE and 32 non-STEVE substorm events. The analysis shows that the magnitude of cross-polar cap potential drop is generally greater for STEVE events. In contrast to non-STEVE substorms, the majority of STEVE events investigated accompany with a pronounced extension of the dawn cell into the pre-midnight subauroral latitudes, reminiscent of the Harang reversal convection feature where the eastward electrojet overlaps with the westward electrojet, which tends to prolong over substorm expansion and recovery phases. This is consistent with the presence of an enhanced subauroral electric field confirmed by previous STEVE studies. The global and localized features of high-latitude ionospheric convection associated with optical STEVE events characterized in this paper provide important insights into cross-scale magnetosphere-ionosphere coupling mechanisms that differentiate STEVE events from non-STEVE substorm events.

High Latitude Ionospheric Electrodynamics During STEVE and non-STEVE Substorm Events

V. Svaldi¹, T. Matsuo², L. Kilcommons², and B. Gallardo-Lacourt^{3,4}

¹Mechanical Engineering Department, Colorado School of Mines, Golden, CO, USA

²Ann & H.J Smead Department of Aerospace Engineering Sciences, University of Colorado, Boulder, CO, USA

³Goddard Space Flight Center, National Aeronautics and Space Administration, Greenbelt, MD, USA

⁴Universities of Space Research Association, Columbia, MD, USA

Key Points:

- First STEVE study focused on global convection patterns shows a strong dawn-cell extending into subauroral pre-midnight sector
- First application of AMGeO to magnetosphere-ionosphere coupling research, involving 32 STEVE and 32 non-STEVE substorms
- Larger cross-polar cap potential drop and more prolonged nightside asymmetry found in STEVE ionospheric convection patterns

Abstract

Previous studies have shown that Strong Thermal Emission Velocity Enhancement (STEVE) events occur at the end of a prolonged substorm expansion phase. However, the connection between STEVE occurrence and substorms and the global high-latitude ionospheric electrodynamics associated with the development of STEVE and non-STEVE substorms are not yet well understood. The focus of this paper is to identify electrodynamics features that are unique to STEVE events through a comprehensive analysis of ionospheric convection patterns estimated from SuperDARN plasma drift and ground-based magnetometer data using the Assimilative Mapping of Geospace Observations (AMGeO) procedure. Results from AMGeO are further analyzed using principal component analysis and superposed epoch analysis for 32 STEVE and 32 non-STEVE substorm events. The analysis shows that the magnitude of cross-polar cap potential drop is generally greater for STEVE events. In contrast to non-STEVE substorms, the majority of STEVE events investigated accompany with a pronounced extension of the dawn cell into the pre-midnight subauroral latitudes, reminiscent of the Harang reversal convection feature where the eastward electrojet overlaps with the westward electrojet, which tends to prolong over substorm expansion and recovery phases. This is consistent with the presence of an enhanced subauroral electric field confirmed by previous STEVE studies. The global and localized features of high-latitude ionospheric convection associated with optical STEVE events characterized in this paper provide important insights into cross-scale magnetosphere-ionosphere coupling mechanisms that differentiate STEVE events from non-STEVE substorm events.

Plain Language Summary

In 2016, citizen observers introduced a mysterious subauroral phenomenon called Strong Thermal Emission Velocity Enhancement (STEVE) to the scientific community. STEVE events are characterized by the presence of a thin and bright purple emission located closer to the horizon than the typical aurora. The focus of this paper is to quantify characteristic features of the global ionosphere during STEVE events, and to investigate their relationship to related phenomena known as substorms using a newly developed data science tool named Assimilative Mapping of Geospace Observation (AMGeO). In this study, using AMGeO, we analyze large amounts of ground-based data during 32 STEVE events as well as 32 non-STEVE substorm events. Findings from the study are helpful to understand differences in the way the magnetosphere is coupled to the ionosphere during STEVE events and non-STEVE substorms.

1 Introduction

In 2016, a Canadian citizen scientist community of auroral photographers introduced a new optical ionospheric phenomenon to the scientific community. Initially referred to as proton arc by the citizen scientists, the optical structure has been named STEVE, a term initially chosen for its lack of scientific implications (Gallardo-Lacourt et al., 2019). To better reflect STEVE's observed physical characteristics, the name was later converted into the backronym, standing for *Strong Thermal Emission Velocity Enhancement*. STEVE is typically observed as a dynamic, thin, westward aligned structure that has bright purple and white emission at subauroral latitudes, equatorward of the auroral oval. STEVE is sometimes accompanied by distinct green finger-like structures known as the "picket fence". Additionally, STEVE is known to be connected to intense subauroral ion drifts (SAIDs) (Archer et al., 2019a; MacDonald et al., 2018). STEVE's emission mechanism has been determined to be different from traditional aurora which are usually associated with energetic electron and ion precipitation (Gallardo-Lacourt et al., 2018; Nishimura et al., 2019). Gillies et al. (2019) have used the newly deployed Transition Region Explorer (TREx) Spectrograph to study STEVE's peculiar mauve emission, and found that STEVE's spectrum corresponds to a continuous emission over 400-800 nm wavelengths. The altitude of STEVE's emission calculated using image triangulation suggests that STEVE occurs between 130-270 km (Archer et al., 2019b; Liang et al., 2019). Taking all these properties into consideration, Harding et al. (2020) have formulated a formation mechanism for STEVE's continuum emission that is distinct from commonly known auroral emission mechanisms. Thanks to these past work, some properties of STEVE are relatively well characterized, however the magnetosphere-ionosphere coupling mechanisms driving these STEVE events are still not completely understood.

The connection between STEVE occurrence and substorms is one of the active research topics in magnetosphere-ionosphere coupling. Previous studies have shown that STEVE occurs at the end of a prolonged expansion phase and that substorms without STEVE are more common than substorm events with STEVE (Gallardo-Lacourt et al., 2018). This indicates that there are unique types of substorms that have the favorable conditions for STEVE to occur (Gallardo-Lacourt et al., 2018; Nishimura et al., 2020). In particular, Nishimura et al. (2020) have analyzed the location of the substorm surge and found that the surge and the injection location rapidly shifts duskward for substorm events when STEVE is observed; while for non-STEVE substorms, the injection location stays around midnight. The authors have also reported that simulation results with the Rice Convection Model with an equilibrated magnetic field model show that the shifting of the injection location contributes to the subauroral polarization streams (SAPS) electric fields becoming narrower and more intense. These results reported in previous studies suggest that although STEVE is not produced by magnetospheric particles precipitating into the Earth's upper atmosphere, the magnetosphere plays a critical role by creating the likely conditions for STEVE to form in the ionosphere.

In this study we analyze the global high-latitude ionospheric response during substorm events with and without STEVE. We utilize the Assimilative Mapping of Geospace Observations (AMGeO) (Matsuo, 2020), available as a newly developed open source data science research tool (AMGeO Collaboration, 2019), to combine ground-based plasma drifts from the Super Dual Auroral Radar Network (SuperDARN) (Chisham et al., 2007) and ground-based magnetic fields from worldwide magnetometers (Gjerloev, 2012). The DMSP SSJ electron precipitation data (Redmon et al., 2017) are also used to determine the conductance. A total of 64 events over the years of 2008-2018, including 32 STEVE events from the study by (Gallardo-Lacourt et al., 2018) and 32 non-STEVE substorm events identified in SuperMAG data base (Newell & Gjerloev, 2011), are investigated using the AMGeO procedure. As an example of AMGeO's capabilities, Figure 1 shows the global ionospheric convection pattern estimated using AMGeO from SuperDARN line-of-sight plasma drift and SuperMAG ground-based magnetometer data along with in-situ measurements of electron

temperature, density and crosstrack ion velocity from the coincident SWARM satellite pass during STEVE occurring on July 25, 2016. Swarm measurements for this event are previously presented in MacDonald et al. (2018). Elevated electron temperature, electron density depletion, and well-defined narrow fast westward plasma flow at peak of optical emission are key signatures of STEVE (Archer et al., 2019a; MacDonald et al., 2018). These key signatures are also present in 8 of the 32 STEVE events investigated in the study by (Archer et al., 2019a). Note that localized westward plasma flows associated with STEVE, reaching as fast as 5.5 km/s, cannot be resolved by AMGeO and that typical plasma drift speed associated with the usual two-cell convection is on the order of 500-1000 m/s. Instead of highly localized plasma flows, this study focuses on global high-latitude ionospheric electrodynamics, so the convection patterns estimated by AMGeO for 64 events are further analyzed using principal component analysis (PCA) to characterize global modes of convection variability associated with STEVE and non-STEVE substorm events. A superposed epoch analysis approach is also used to determine correlations of the time-varying magnitude of principal components (PC) to solar wind parameters and geomagnetic activity indices for both categories of events.

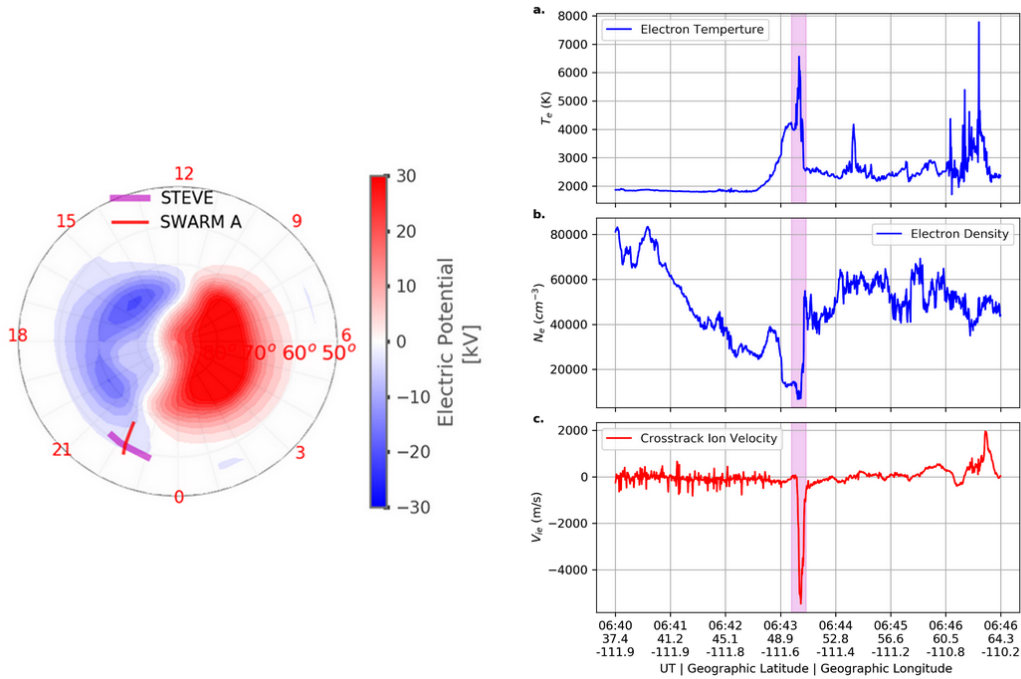


Figure 1. (Left) Global ionospheric convection pattern estimated by AMGeO, with overlays of STEVE locations as reported by ground-based instruments and observers in the pre-midnight sector (magenta), and Swarm A satellite track (red). (Right) Swarm A satellite in-situ measurements along the pass on July 25, 2016 that coincides with STEVE optical emission: a.) Electron temperature; b.) Electron number density; and c) Ion velocity (positive value is eastward flow).

The paper is structured as follows. Following a description of STEVE and non-STEVE substorm event selections, data sets and data analysis approaches, including assimilative mapping, principal component analysis and superposed epoch analysis, used in this study are given in Section 2, results from comparative analysis of STEVE and non-STEVE substorm convection patterns estimated by AMGeO are presented in Section 3. Section 4 summarizes key differences between STEVE and non-STEVE substorm events identified in Section 3 as tables. Discussion and conclusions are given in Sections 5 and 6.

2 Data Set and Data Analysis Approach

This section provides details pertaining to the STEVE and non-STEVE substorm events, data, and data analysis approaches used in this study. Section 2.1 discusses the events selected including the specific dates and onset times in UT for all STEVE and non-STEVE substorm events occurring between the years 2008 and 2018. Section 2.2 explains the assimilative mapping procedure and data ingested in order to generate assimilative maps of high-latitude ionospheric convection patterns. Post analysis techniques performed, including principal component analysis, superposed epoch analysis, and reconstruction of electrostatic potential distribution, are described in Section 2.3.

2.1 Event Selection over 2008-2018

The 32 STEVE events investigated in this study are identified using the Time History of Events and Macroscale Interactions during Substorms (THEMIS) and the Redline Geospace Observatory (REGO) groundbased AllSky Imagers (ASIs) managed by the University of Calgary (GallardoLacourt et al., 2018). Table 1 shows a list of these events, occurring between the years of 2008 and 2018. 28 of these events are previously investigated by GallardoLacourt et al. (2018) wherein 21 events are identified by THEMIS ASI and 7 by REGO ASI. The 4 additional STEVE events are identified using REGO ASI data. The start time of the STEVE events (as shown in Table 1), hereafter referred to as the STEVE optical onset, is the UT time at which STEVE is first detected in the optical data from the THEMIS and REGO ASIs (GallardoLacourt et al., 2018). In ASI images, STEVE optical features appear as its distinct long, narrow structure located equatorward of the auroral oval. One important aspect to consider is that STEVE optical onset time definition is limited by the camera field-of-view. Since STEVE is a westward moving structure, it is possible that the initial formation of STEVE could occur eastward of the camera field-of-view. This may lead to a potential time difference between STEVE's real onset and what is defined here as STEVE optical onset. Nevertheless, since STEVE propagates rapidly westward this timing ambiguity should not significantly affect our results.

Table 1. List of dates and UT onset times of 32 STEVE events identified optically using ASI (GallardoLacourt et al., 2018).

Event	Date	STEVE Onset	Event	Date	STEVE Onset
1	2-11-2008	9:30	17	2-20-2012	8:40
2	3-26-2008	7:20	18	9-13-2013	8:30
3	3-27-2008	3:00	19	8-21-2014	9:20
4	3-28-2008	2:00	20	9-7-2015	5:35
5	3-28-2008	7:22	21	9-11-2015	5:20
6	4-12-2008	8:00	22	2-8-2016	6:30
7	5-4-2008	8:00	23	4-17-2016	5:10
8	7-12-2008	3:40	24	7-25-2016	6:00
9	3-11-2010	6:00	25	7-29-2016	5:20
10	4-4-2010	7:20	26	8-22-2017	3:08
11	4-5-2010	5:30	27	8-24-2017	6:11
12	8-3-2010	5:40	28	9-18-2017	6:35
13	9-17-2010	7:00	29	9-27-2017	6:41
14	4-2-2011	6:47	30	3-25-2018	7:46
15	4-20-2011	8:38	31	4-10-2018	5:10
16	6-23-2011	7:00	32	7-17-2018	6:30

Event dates with top 10 greatest minimum SML values are highlighted in red

The 32 non-STEVE substorm events are selected, using the SuperMAG substorm database, from the Newell and Gjerloev (2011) substorm list which covers a time range from 1969 to the current. Substorms that have occurred in the absence of STEVE are selected as control events so that non-STEVE substorms have the same relative month, year, and onset UT time as the STEVE events as indicated by dates and times for all 64 events listed in Tables 1-2). These STEVE and non-STEVE substorm events are both analyzed every 5 minutes for a 3 hour duration, including 1.5 hour prior and 1.5 hour post the onset time using the same data analysis approach described next.

The mean and minimum values of SML, which is the SuperMAG version of the AL-index available at a 1-min cadence (Newell & Gjerloev, 2011), are also considered in the selection of non-STEVE substorm events. The variability in SML mean, minimum and standard deviation for STEVE and non-STEVE substorm events are shown in Figure 2. While the average of SML minimum value for STEVE events is -727 nT with a standard deviation of 220 nT, it is -605 nT with a standard deviation of 176 nT for non-STEVE substorm events. The minimum SML values for these two categories of events differ by 122 nT on average. Both the official auroral electrojet indices or AL-index and the SuperMAG variation referred to as the SML-index are examined in this study. Note that there are several differences that exists between the two indices. For example, there is a total of 12 ground based magnetometer stations that are used for the official auroral electrojet indices ($AE = AU - AL$), whereas over 100 magnetometer stations in collaboration with SuperMAG are used to derive the SuperMAG auroral electrojet indices ($SME = SMU - SML$) (Newell & Gjerloev, 2011). There is also a lack of AL-index data availability for events occurring in 2018. The average minimum AL-index magnitude for STEVE events, excluding events occurring in 2018, is -614 nT with a standard deviation of 192 nT, and the average minimum AL-index magnitude for non-STEVE substorms is -519 nT with a standard deviation of 268 nT.

The substorm onset UT times, listed in Table 2, are identified in Newell and Gjerloev (2011) using the satisfaction of the following SML criteria: the sharp initial SML drop more than 45 nT in 3 minutes and the sustained SML drop (meaning 100 nT below the average value for the duration of 25 minutes that starts 5 minutes after the onset). If these conditions are met, the substorm onset is set at the last minute before a 15 nT drop in SML (Newell & Gjerloev, 2011). Substorm phases have been identified by using the standard definition according to the AL-index's slope (Kivelson & Russell, 1995). The growth phase is typically identified by the initial interval of growing AL; while later, during the expansion phase, AL rapidly decreases. Eventually AL reaches a minimum and then the index values start increasing. This period of increasing AL is usually known as the substorm recovery phase. An excellent example of the AL-index behaviour during substorms is presented in Figure 13.19 of Kivelson and Russell (1995). It is important for the reader to remember that, although SML index is calculated using more stations than the classical AL-index, both indices represent the level of disturbance in the westward auroral electrojet recorded by magnetometers.

2.2 Assimilative Mapping Analysis

The AMGeO procedure is used to generate assimilative maps of high-latitude electrodynamic variables by combining ground-based plasma drift and magnetic field observations with empirical models of ionospheric convection and aurora (Cousins & Shepherd, 2010; Newell et al., 2009) as described in Matsuo (2020). Assimilative maps of high-latitude electrodynamics variables including electrostatic potential (ionospheric convection), Pedersen and Hall conductance, and Joule heating are produced every 5 minutes for 3 hours for each event listed in Section 2.1. Only AMGeO maps of electrostatic potential are presented in this paper. These AMGeO electrostatic potential maps display equipotential contour lines, marking convective motion of ionospheric plasma, in the geomagnetic latitudes and geomagnetic local time coordinates, from 90 to 50 magnetic latitudes with geomagnetic local noon

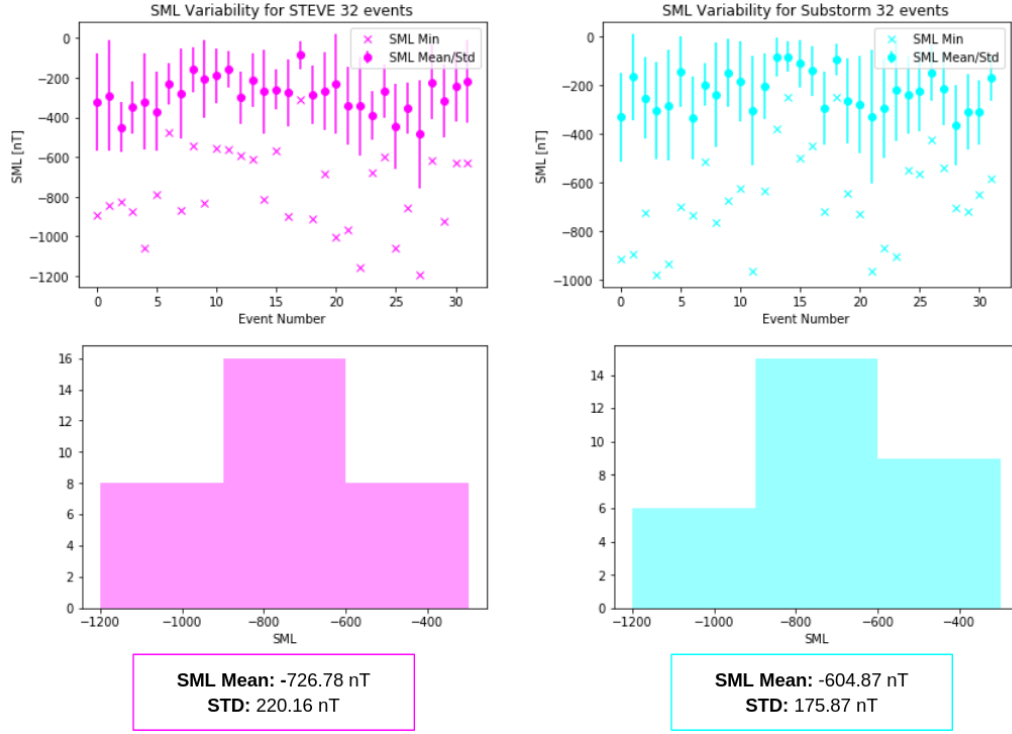


Figure 2. Top: Variability in the SML-index minimum and mean values for all 32 STEVE events (pink) and 32 non-STEVE substorm events (blue) Bottom: Histogram of SML-index minimum values for all 32 STEVE events (pink) and 32 non-STEVE substorm events (blue).

(12) at the top and midnight (0) at the bottom. The AMGeO's spatial resolution is 2.5 degrees in latitude and 15 degrees in longitude. This is not high enough resolution to resolve narrow westward plasma flows usually associated with STEVE events in pre-midnight subauroral latitudes, as shown for the SWARM ion drift (Figure 1 (c)).

The magnetic field observations ingested to AMGeO are ground-level magnetic perturbations from the SuperMAG data service which collects, standardize, and distribute data from more than 300 ground-based magnetometers worldwide (Gjerloev, 2012). Additional data ingested include the line-of-sight ionospheric plasma drift observations from the SuperDARN (Chisham et al., 2007). Ingesting ground-based magnetometer observations into AMGeO requires an estimate of height-integrated ionospheric conductivity or conductance. Following McGranaghan et al. (2016), we used an optimal interpolation approach to specify the Hall and Pedersen conductance. The data used for this purpose include pseudo conductance observations created by DMSP SSJ particle precipitation as described in McGranaghan et al. (2015). The conductance used for this study thus differs from the default conductance maps used in AMGeO, which is derived from Ovation Prime electron precipitation model (Newell et al., 2009).

2.3 Principal Component Analysis (PCA) and Superposed Epoch Analysis

To characterize global modes of variability of ionospheric convection associated with STEVE as well as non-STEVE substorm events, AMGeO maps of electrostatic potential are further analyzed using PCA. The mean convection map is first computed from assimilative maps generated for the 32 STEVE events, which is then subtracted from each map to generate residual maps. These residual maps are aggregated over time across all events and

Table 2. List of dates and UT onset time of 32 non-STEVE substorm events selected using the SuperMAG substorm database (Newell & Gjerloev, 2011).

Event	Date	Substorm Onset	Event	Date	Substorm Onset
1	2-11-2008	16:58	17	6-24-2011	7:09
2	3-26-2008	21:37	18	2-25-2012	11:26
3	2-11-2008	1:15	19	9-16-2013	14:46
4	3-12-2008	6:31	20	8-12-2014	20:14
5	3-18-2008	2:44	21	9-10-2015	16:29
6	3-10-2008	4:53	22	9-14-2015	15:01
7	4-6-2008	4:37	23	2-18-2016	2:56
8	3-10-2008	22:39	24	4-23-2016	21:03
9	3-29-2008	20:28	25	7-23-2016	5:01
10	3-12-2010	4:56	26	7-28-2016	4:05
11	3-20-2010	7:25	27	8-7-2017	8:18
12	4-7-2010	6:29	28	8-27-2017	15:53
13	4-8-2010	1:38	29	9-27-2017	12:14
14	9-9-2010	12:16	30	9-29-2017	11:25
15	9-15-2010	6:38	31	5-9-2018	4:26
16	4-24-2011	22:40	32	7-24-2018	5:45

Event dates with top 10 greatest minimum SML values are highlighted in red

used to compute a sample covariance that represents variability of ionospheric convection during STEVE events. The eigenvalue decomposition of this sample covariance matrix yields principal components as empirically determined eigenvectors. Each principal component is an independent orthogonal mode of variability from the mean. Principal components (PC) are ordered according to the percentage of variance that is attributed to each component. Once these global modes of variability of ionospheric convection are determined, the time-varying magnitudes of PC are computed from residual maps by linear regression, which are referred to as PC coefficients. The same PCA analysis steps are applied to assimilative maps generated for the 32 non-STEVE substorm events.

To examine the timing of temporal variation of PC coefficients and solar wind parameters and geomagnetic activity indices (including the AL-index, AU-index, IMF By and Bz parameters, and cross-polar cap potential), a correlation analysis and a superposed epoch analysis are further applied. Each time series, spanning from 1.5-hour prior to the STEVE optical onset (or substorm onset), to 1.5-hour post the STEVE optical onset (or substorm onset), is divided into quarter-hour increment bins. The center bin labeled at time zero is the bin in which the substorm onset time (or STEVE optical onset time) is included. The correlations between PC coefficients, AL-index, AU-index, IMF By/ Bz solar wind parameters, and cross-polar cap potential are computed using the spearman correlation function from the Python SciPy library. Aurora electrojet indices (AL and AU index), and Interplanetary Magnetic Fields (IMF) By and Bz obtained from OMNI database at 1-minute cadence are used.

3 Data Analysis Results

This section presents both quantitative and qualitative analysis results of AMGeO electrostatic potential maps obtained for 32 STEVE events and 32 non-STEVE substorm events as described in Section 2. These analysis results help characterize global high-latitude ionospheric convection features associated with STEVE events and non-STEVE substorm events. Section 3.1 introduces representative features of the dawn-dusk asymmetry or dawn-

cell extension found, in a varying degree, among individual 32 STEVE events. Differences in the mean convection patterns and cross-polar cap potential are evaluated between the two categories of events in Section 3.2. In Section 3.3 the dawn-cell extension morphology observed in AMGeO maps is further examined in terms of the leading modes of global ionospheric convection variation associated with STEVE events as well as correlation of each mode's amplitude with solar wind parameters, and geomagnetic indices. Section 3.4 investigates the same for non-STEVE substorm events in order to contrast the differences in the ionospheric convection's characteristic behaviors found for 32 STEVE events from those behaviours identified for 32 non-STEVE substorm events that occur without the presence of STEVE. The median PC coefficient trend, that represents a typical temporal variation of these modes for all 32 STEVE and 32 non-STEVE substorm events, as well as the electrostatic potential maps reconstructed with the PC and median PC coefficient for both categories of events are described in Section 3.5. In addition to typical temporal behaviors of leading modes, Section 3.6 further investigates the dawn-cell extension and evaluates the temporal trends of PC coefficients and AMGeO electrostatic potential maps for 10 individual STEVE and 10 non-STEVE substorm events. A case study for STEVE event occurring on March 26, 2008 and its comparison to a non-STEVE substorm event occurring on September 14, 2015 are presented in Section 3.7. An overall comparison of characteristic features of high-latitude electrodynamics between STEVE events and non-STEVE substorm events is summarized in Section 4.

3.1 Dawn-Dusk Asymmetric Ionospheric Convection Patterns Found in STEVE Events

For 27 of the 32 STEVE events investigated, a strong dawn-cell extension, identified as the westward penetration of the dawn cell into the pre-midnight sector in the vicinity of subauroral latitudes, is observed in the AMGeO maps. An example of an AMGeO spatial distribution map displaying this strong dawn-cell extension during a STEVE event can be viewed in Figure 3. Four of the 32 STEVE events have displayed a weaker dawn-cell extension. Specific STEVE event dates that displayed a weak dawn-cell extension can be found in Supplemental Materials Table S1. There is a dawn-cell extension associated with non-STEVE substorm events (Section 3.4), however the magnitude and morphology differences of this feature make it distinguishable from STEVE events. It should be noted that in the context of this study subauroral latitudes indicate magnetic latitudes below about 70 degrees and the term "subauroral latitudes" is not referring to the auroral boundaries defined by precipitating auroral particles. As noted in the introduction, AMGeO cannot resolve the narrow fast flows of ion drifts directly associated with STEVE. The focus is therefore rather on the localised convection patterns with a reminiscence to the Harang reversal wherein that is spatially collocated with STEVE optical emissions.

3.2 Mean Ionospheric Convection for STEVE and non-STEVE Substorm Events

The mean convection pattern is estimated for each category of events from AMGeO maps produced at 5-minute cadence for each 3-hour duration of all 32 STEVE and 32 non-STEVE substorm events. Figure 4 (a) is the mean convection pattern for STEVE events, with a cross-polar cap potential of 48.15 kV, and shows the dawn cell slightly extending past the midnight boundary into the pre-midnight sector between 75 and 65 degrees magnetic latitude. In comparison, Figure 4 (b) shows the mean convection pattern for non-STEVE substorm events. The mean convection pattern for non-STEVE substorm events is noticeably weaker than the mean convection found for STEVE events, with a cross-polar cap potential of 39.32 kV. The extension of the dawn cell observed in the mean convection pattern for STEVE events is also slightly more prominent and further extending into the pre-midnight sector. The physical implications of this enhanced electrostatic potential during STEVE-events is addressed later in Section 5.

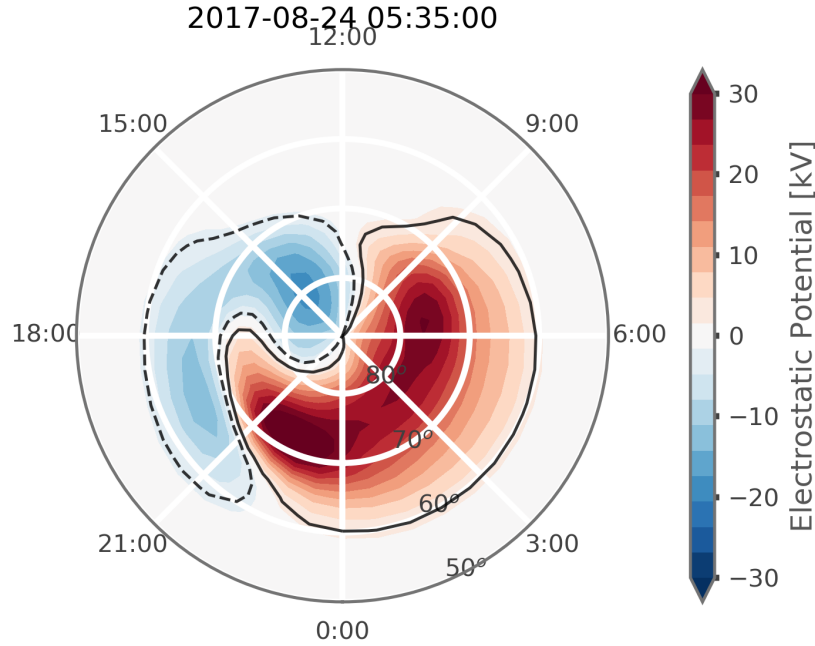


Figure 3. AMGeo map for STEVE event occurring on August 8th, 2017 at 5:35 UT that displays a strong dawn-cell extension penetrating into the dusk cell, reaching past the pre-midnight sector, near subauroral latitudes.

3.3 Global Modes of Ionospheric Convection Variability Associated with STEVE Events

A strong dawn-cell extension observed in the majority of the STEVE events, as introduced in Section 3.1), is further examined in terms of the global modes of variability about the mean convection pattern shown in Figure 4 (a) in Section 3.2. Figure 5 displays the maps of the first four modes, noted here as PC1 through PC4. The map of PC1 (Figure 5 (a)) appears to be a dawn-cell intensification mode and explains 51.6 percent of the total variance of the ionospheric convection assimilative maps estimated for 32 STEVE events. PC2 (Figure 5 (b)) also has a significant explained variance of 23.4 percent, and its two-cell pattern shows a dawn-cell penetrating into the dusk cell around 65 degrees magnetic latitude in the pre-night sector, characterizing a localized nightside dawn-cell penetrating mode. PC3 (Figure 5 (c)) exhibits a considerable nightside asymmetrical pattern which seems to correspond to a mode of variability associated with the dawn cell extending very far westward into and past the pre-midnight sector. PC3 is thus referred to as the dawn-cell extension mode or STEVE mode and has an explained variance of 7.9 percent. PC4 has low explained variance, contributing less than 5 percent of the overall variance in all STEVE events and is referred to as a weak asymmetry mode. Among these four principal components, PC2 and PC3 (Figure 5 (b)-(c)) are of particular interest for this study as these modes visually represent the westward dawn-cell extension into the pre-midnight sector.

Superposed epoch analysis of time-varying PC coefficients and cross-polar cap potential is shown in the pink colored box-plots in Figure 6 over 1.5 hour prior to and 1.5 hour post substorm onset. Superposed epoch analysis of AL-index, AU-index, IMF By, and IMF Bz is included to examine the relationship of global modes of ionospheric convection evolution to solar wind drivers and overall substorm evolution indicated by geomagnetic indices. The

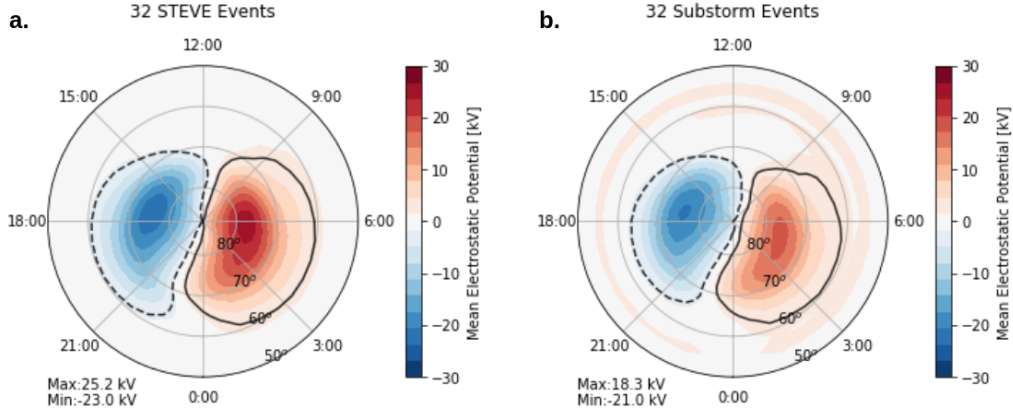


Figure 4. a.) Mean electrostatic potential distribution from 32 STEVE events. The cross- polar cap potential is 48.15 kV. The maximum and minimum potential values are 25.2 kV and -23.0 kV, respectively. b.) Mean electrostatic potential distribution produced using 32 non-STEVE substorm events. The cross-polar cap potential was calculated to be 39.32 kV. The maximum and minimum potential values are 18.3 kV and -21.0 kV, respectively

correlations between PC coefficients, AL-index, AU-index, IMF By, IMF Bz, and cross-polar cap potential are summarized in Figure 7. IMF, AL and AU are obtained from the NASA OMNI database. The median of PC1 coefficients changes signs from negative to positive close to the time of substorm onset marked by the blue vertical line at 0.0 hour (Figure 6 (a)). At the time of this sign change there is also an intensification observed in the magnitude of the dawn cell in terms of electrostatic potential values which can be visualized in Section 3.5 Figure 11.

There is a significant negative correlation at -0.65 between PC1 coefficient and IMF By, so the changes of PC1 mode are partly attributed to the changes of IMF By. The median of PC2 coefficients, representing a localized nightside dawn cell penetrating mode, maximizes at the time of substorm onset (Figure 6 (b)). The median of PC3 STEVE mode coefficients also changes signs, close to the substorm onset, from negative to positive (Figure 6 (c)). The median of PC3 coefficients reaches its maximum at 0.5 hour post substorm onset, corresponding to the time when the dawn-cell extends into the pre-midnight sector most. This coincides with the end of expansion phase and beginning of recovery phase as well as with the time of the STEVE optical onset, which is consistent with the STEVE onset timing reported in GallardoLacourt et al. (2018).

The median magnitude of IMF By and Bz is very small and predominantly negative for the entire 3-hour duration of superposed epoch analysis (see Figure 6 (g)-(h)). The superposed epoch analysis of AL-index (Figure 6(e)) shows that the minimum of median AL at -410 nT occurs 0.5 hour after the substorm optical onset, marking the end of expansion phase and beginning of recovery phase. The median cross-polar cap potential is seen to maximize at 62.8 kV, at 0.5 hour post substorm onset in the recovery phase (Figure 6 (f)). The cross-polar cap potential also has significant negative correlation with PC1 coefficient of -0.67 and with PC2 coefficient of 0.66 (Figure 7). The AL-index negatively correlates with PC2 coefficient at -0.53, and PC3 shows a small negative correlation of -0.28 to the AL index. The STEVE mode associated with the dawn-cell extension (PC3) has no other significant correlations, except for a slight positive correlation to IMF Bz at 0.21. This dawn-cell extension is found to be unrelated to IMF By, which is largely in agreement

with the past studies. For instance, the previous work using SuperDARN data have found that a typical IMF Bydependent dawn-dusk asymmetry is seen over the entire convection pattern during the substorm growth phase but during the expansion phase this asymmetry is confined only in the polar cap and dayside (Grocott et al., 2010).

The average duration of the optical STEVE phenomenon in the 32 events investigated is found to be 1 hour with a standard deviation of 34 minutes. For the 27 STEVE events with a detectable strong dawn-cell extension in the pre-midnight sector, the average optical STEVE event duration is 1 hour 16 minutes. These are largely consistent with the STEVE duration of 1 hour as reported in GallardoLacourt et al. (2018). The dawn-cell extension found from these 27 events lasts 1 hour and 12 minutes on average, which is about the same duration of optical STEVE events. Note that no apparent event-by-event correlation is found between the durations of the dawn-cell extension and the optical STEVE event, even though the average durations are similar.

3.4 Global Modes of Ionospheric Convection Variability Associated with Non-STEVE Substorms

Figure 8 shows the first four leading global modes of variability for 32 non-STEVE substorms events. These modes represent spatially coherent variability about the mean convection pattern shown in Figure 4 (b). The PC maps for the non-STEVE substorm events are generally similar to the PC maps for STEVE events (Figure 5 (a)-(d)) with the exception of PC3. PC1 represents a dawn-cell intensification mode like PC1 for STEVE events, and has an explained variance of 46.3 percent and shows significant correlation to IMF By and Bz (Figure 10). PC2 has an explained variance of 25.2 percent and shows a two-cell spatial distribution with the dawn cell penetrating into the dusk cell in the pre-midnight sector in a similar fashion to the localized nightside dawn-cell penetrating mode found for STEVE events (Figure 8 (b)). PC3 appears to represent a dawn-cell extension mode for non-STEVE substorms (Figure 8 (c)), exhibiting an asymmetrical pattern associated with the dawn-cell westward extension into the pre-midnight sector on nightside. However, a close inspection of PC3 for non-STEVE substorm events, which has an explained variance of 7.2 percent, shows that the extent of dawn-cell extension is not as prominent as PC3 for STEVE events (Figure 5 (c)). PC4 has the lowest explained variance contributing about 5 percent of overall variance in all non-STEVE substorms events and is referred to as a weak asymmetry mode (Figure 8 (d)).

Superposed epoch analysis of the PC coefficients, AL-index, AU-index, IMF By and Bz, and cross-polar cap potential for non-STEVE substorm events are shown in the blue colored box-plots shown in Figure 9. The blue vertical line at 0.0 hour marks the substorm onset at when superposed epoch analysis is centered. PC coefficients for the substorm events are correlated to solar wind parameters and geomagnetic activity indices in the same manner as for STEVE events (Figure 10). In the superposed epoch analysis, the median of PC1 coefficients for 32 non-STEVE substorm events is seen to change signs from negative to positive around the time of substorm onset (Figure 9 (a)). The median of PC2 coefficients, representing a localized nightside dawn-cell penetrating mode of variation, maximizes slightly after time of substorm onset around 0.25 hour (Figure 9 (b)). The median of PC3 coefficients change signs close to the substorm onset going from negative to positive (Figure 9 (c)). The timing of the maximum of PC3 coefficients directly corresponds to the peak of dawn-cell extensions into the pre-midnight sector as confirmed in the electrostatic potential maps.

The median of IMF By is very small in magnitude and predominantly positive for the 3-hour duration of the superposed epoch analysis (Figure 9 (g)). Note that the median of IMF By is predominantly negative for STEVE events (Figure 6 (g)). The median IMF Bz varies from nearly zero at 1.5 hour prior to onset and decreases to about -3 nT at substorm onset followed by the slow return to zero over 1.5 hours post substorm onset (Figure 9 (h)).

The temporal trends of By and Bz over the 3-hour duration of superposed epoch analysis are generally smoother for non-STEVE substorm events in comparison to STEVE events. There is notable negative correlation between PC1 coefficient and IMF By (-0.62) and between PC1 coefficient and IMF Bz (-0.44). The AL magnitude for non-STEVE substorm events is smaller when compared to STEVE events. These results are consistent with the superposed epoch analysis of the AL-index from GallardoLacourt et al. (2018) in which the AL magnitude for STEVE events was observed to be higher than observed for regular non-STEVE substorms. The cross-polar cap potential for non-STEVE substorm events is also significantly weaker in magnitude across the 3-hour duration of the superposed epoch analysis compared to STEVE events.

3.5 Reconstructed Ionospheric Convection Maps for STEVE and Non-STEVE Substorm Events

The mean convection map, PC maps, and the median values of PC coefficients, described in Sections 3.2-3.4, are used to reconstruct a time series of electrostatic potential maps at 0.5 hour cadence over 3 hours from 1.5-hour prior through 1.5-hour post substorm onset time for both categories of events. The median values for PC coefficients are also graphed relative to substorm onset time to investigate temporal trends in global ionospheric convection patterns and to identify the differences between two categories of events as shown in Figure 11, from the top to bottom, at three key time frames at 30 minutes before and after as well as at time of substorm onset. These reconstructed ionospheric convection maps reflect typical spatiotemporal variability of convection patterns derived from the results of PCA and superposed epoch analysis of AMGeO maps, and provide helpful insight into the timing and duration of the dawn-cell extension development relative to substorm onset. Black contour lines are added to demarcate the boundaries of positive and negative cells in order to aid in the visualization of the dawn-cell extension into the pre-midnight sector.

Prior to the substorm onset time, there is a slight westward extension of the dawn cell visible for both STEVE and non-STEVE substorm events (Figure 11 (top)). At this time, PC1-PC3 coefficients are all growing in magnitude for both STEVE and non-STEVE events. At substorm onset, shown in Figure 11 (middle), there is a change in the sign of PC1 and PC3 coefficients relating to an intensification of the dawn cell as observed in reconstructed electrostatic potential maps for both categories of events. The enhancement of the dawn cell is noticeably greater in magnitude for STEVE events compared to non-STEVE substorm events. Figure 11 (bottom) displays maps reconstructed at 30 minutes after substorm onset. The median value of PC3 coefficients peaks at this time which is the point of the greatest dawn-cell extension among three time frames shown in Figure 11. The dawn-cell extension into the pre-midnight sector for STEVE events is more pronounced more clearly extending into the dusk cell, whereas the dawn-cell extension for non-STEVE substorm events is visibly weaker in magnitude. The temporal trend of PC1 coefficients after substorm onset is distinctively different for STEVE and non-STEVE substorm events. For non-STEVE substorm events all PC coefficients, including PC1 (dashed red line,) are approaching zero reflecting the return of a symmetric two cell convection pattern towards the end of the recovery phase. For STEVE events the median values of PC2, PC3, and PC4 coefficients all approach or reach zero after one hour post substorm onset. However, the median of PC1 coefficients (solid red line) continues to grow even after substorm onset, contributing to the prolonged dawn-dusk asymmetry on nightside visible in convection patterns for STEVE events.

3.6 Dawn-cell Extension in Individual STEVE and Non-STEVE Substorm Events

The dawn-cell extension is further investigated by closely evaluating the temporal trends of PC coefficients and AMGeO electrostatic potential maps for 10 STEVE and 10 non-STEVE individual substorm events that are selected based on the peak magnitude of min-

imum SML values (see event dates denoted in red for STEVE events in Table 1 and for non-STEVE substorm events in Table 2). Figure 12 shows AMGeO electrostatic potential maps for these 10 STEVE events at the time the greatest dawn-cell extension suggested by the maximum time of PC3 coefficients. A strong dawn-cell extension is visible in the pre-midnight sector near subauroral latitudes for 9 out of the 10 events except for the STEVE event occurring on February 8, 2016 (Figure 12 (f)).

The temporal trends observed in PC coefficients of these 10 individual STEVE events are consistent with the overall trends seen in the median of PC coefficients for all 32 STEVE events (Figure 6). For these 10 events, the magnitude of PC1, which is characterized as the dawn-cell intensification mode in Section 3.3, exhibits a strong negative correlation with IMF By at -0.71 with the sign changes coinciding with changes in the IMF By orientation. The overall temporal evolution of PC1 coefficients for the 10 events is also related to AL and IMF Bz as for all 32 STEVE events (Figure 7). PC1 coefficients increase in magnitude prior to substorm onset during the growth phase for all 10 events, and do not approach or reach zero during the recovery phase for 7 out of 10 events. In addition, in 9 out of 10 events, there is a significant amount of dawn-dusk asymmetry with a dawn-cell extending into the pre-midnight sector about 1.5 hours after substorm onset, well into the recovery phase. The localized nightside dawn-cell penetrating mode (PC2) is also seen to increase during the growth phase prior to substorm onset and has some correlation with IMF Bz, IMF By and AL at -0.47, 0.34, -0.49. See Figure 7 for correlation for all 32 STEVE events. Correlation matrix and superposed epoch analysis for 10 STEVE events with strongest SML is provided in supplementary material. The peak time of PC2 coefficients for these individual events has a lot of variability, for 6 out of 10 events occurring in the expansion phase and for 4 of 10 events occurring in the recovery phase. The AMGeO electrostatic potential maps at the time of PC2 coefficient maximum show a strong dawn-dusk asymmetry in 10 out of the 10 events, similar to the morphology of PC2 (Figure 5 (b)) where the dawn cell is extended past the midnight boundary penetrating the dusk cell. The primary mode of variability associated with the westward extension of the dawn-cell into the pre-midnight sector is PC3 as seen in the morphology of AMGeO electrostatic potential maps shown at the time of PC3 coefficients' maximum in Figure 12 (a-e, g-h). The magnitude of PC3 grows in magnitude prior to substorm onset for all 10 events, and continues into the recovery phase for some events. The PC3 coefficient peak time has some variability for individual events, but for the majority (7 out of 10 events) the maximum of PC3 coefficient occurs in the recovery phase and for the remaining events it occurs during the expansion phase. There are no notable temporal trends of the magnitude of PC4 that is the weak asymmetry mode, as the coefficients are small in magnitude and remain largely close to zero.

There are differences and similarities between these individual STEVE events and non-STEVE substorm events in terms of the morphology of ionospheric convection patterns at the time of PC3 coefficient peak and temporal evolution of PC1-PC4 coefficients. One of the most notable differences is that the dawn-cell extension for non-STEVE substorm events is typically not as far extended into the pre-midnight sector as for STEVE events, more localized around midnight. It typically lasts from the growth phase through the end of expansion phase, fading completely by the end of expansion phase for 7 out of 10 non-STEVE substorm events. For these 10 non-STEVE substorm events, PC1 coefficients have a strong negative correlation with IMF By and IMF Bz at -0.43 and -0.53, respectively. See Figure 10 for correlation for all 32 non-STEVE substorm events. Correlation matrix and superposed epoch analysis for 10 non-STEVE substorm events with strongest SML is provided in supplementary material. As for 10 STEVE events, PC1 coefficients increase in magnitude more rapidly during the substorm onset or right after onset during the expansion phase for all 10 events. Unlike for STEVE events, PC1 coefficients typically approach or reach zero during the recovery phase, returning to a symmetrical two-cell convection patterns about 1.5 hours after the substorm onset during the recovery phase (7 out of 10 non-STEVE substorm events). PC2 coefficients increase in magnitude during the growth phase prior to the substorm onset and has some correlations to IMF Bz, IMF By, and AL at -0.30, 0.40, -

0.41. This behavior is similar between individual STEVE and non-STEVE substorm events. The peak time of PC2 coefficients has a lot of variability among these 10 events, occurring in the growth phase for 3 out of 10 events, in the expansion phase for 4 out of 10 events, and in the recovery phase for 3 of 10 events. The AMGeO electrostatic potential maps at the time of PC2 coefficient maximum show a strong dawn-dusk asymmetry in 10 out of 10 events in a similar fashion to STEVE events. Unlike STEVE events, the PC3 coefficients increase in magnitude post substorm onset for non-STEVE substorm events. The PC3 coefficient peak time has some variability among individual events, but for the majority (6 out of 10 events) PC3 coefficients reaches their peak at the end of the expansion phase. For the remaining events, it occurs during the beginning of the recovery phase. The morphology of AMGeO electrostatic potential maps at the time of PC3 coefficients maximum has a dawn-cell extension into the pre-midnight sector in 10 out of the 10 events as shown in Figure 13. The maximum of PC3 coefficients correlates to the maximum of dawn cell intensification and westward extension. It can be noted that this dawn cell extension is less pronounced and more diversified when compared to the dawn cell morphology observed in STEVE events. As for STEVE events, there is nothing notable aspects about PC4 coefficients for individual non-STEVE events. See Figure 9) for the overall temporal trends of the median PC coefficients for all 32 non-STEVE substorm events.

3.7 Case Study Events: STEVE Event March 26, 2008 vs non-STEVE Substorm Event September 14, 2015

Key differences in global high latitude electrodynamics between STEVE and non-STEVE substorm events are discussed for two specific case study events: the STEVE event occurred on March 26, 2008 (Figure 14) and the non-STEVE substorm event occurred on September 14th, 2015 (Figure 15). These events are chosen for comparison as they have similar SML minimum values. In addition, this STEVE event has been investigated in detail by Nishimura et al. (2020).

The AMGeO electrostatic potential maps for the STEVE event on March 26th, 2008 are shown in Figure 14, from 6:00 UT to 9:15 UT in 5-minute intervals during the STEVE optical event (from 7:20 UT to 8:00 UT) otherwise in 15-minute intervals, with maps at substorm onset at 6:30 UT as marked with a black dotted box and at STEVE optical onset at 7:20 UT marked with a pink dotted box. The SML minimum value for this event is -826 nT at 7:20 UT, occurring at the end of the expansion phase and the beginning of the recovery phase, which is indicated by a black solid box. A slight westward extension of the dawn cell can be observed at 6:00 UT. As time progresses the dawn cell becomes more enhanced and extending further into the pre-midnight sector. The maximum of the dawn-cell extension, which occurs when PC3 coefficients are maximized, can be seen at 7:20 UT, which is also the STEVE optical onset and beginning of substorm recovery phase. After reaching the maximum, the magnitude of the dawn-cell extension decreases and a mostly symmetric two cell convection pattern can be observed 1 hour and 25 minutes into the recovery phase at 8:45 UT.

For comparison, the AMGeO electrostatic potential maps for the non-STEVE substorm event on September 14th, 2015 are shown in Figure 15 from 14:00 UT to 17:15 UT. Maps are displayed in 15 minute intervals from 14:00 UT through 15:00 UT prior to substorm onset and from 16:00 UT through 17:15 UT after substorm onset and in 5 minute intervals otherwise, with maps at the substorm onset (15:00 UT) marked with a black dotted box and at the time of SML minimum (15:40 UT) marked with a black solid box in Figure 15. The SML minimum value for this event is -935 nT. Here, there is also a slight and weak extension of the dawn cell present one hour prior to the substorm onset at 14:00 UT. The dawn cell extension becomes more prominent as time progresses but it is not as far extended into the pre-midnight sector as observed for the STEVE event in Figure 14. The maximum time of the dawn cell extension occurs at the PC3 coefficient maximum at 15:40 UT. After this time the dawn cell extension decreases and a more dawn-dusk symmetric convection pattern is

observed approximately 50 minutes into the recovery phase of the substorm at 16:30 UT. In this non-STEVE substorm event, the dawn cell extension has a shorter duration than that observed for the STEVE event. The potential physical implications of this difference is addressed later in the discussion section.

Upon a visual inspection, the westward extension of the dawn cell that is present in AMGeO electrostatic potential maps for the STEVE event on March 26, 2008 shows a resemblance in its shape and location to the westward surge reported by Nishimura et al. (2020) for the same STEVE event. Nishimura et al. (2020) have concluded that for STEVE events the intense upward field-aligned currents and substorm surge reach further into the dusk sector, while for non-STEVE substorms are localized at midnight (Nishimura et al., 2020). Both of the STEVE events included in the Nishimura et al. (2020) study are in fact included in the list of 32 STEVE events investigated in this study. The AMGeO convection patterns for March 26, 2008 and April 5, 2010 both displayed a strong dawn-cell extension. Qualitative similarities are observed between the westward dawn-cell extension and the westward substorm surge seen in results from Nishimura et al. (2020). From a visual comparison of AMGeO electrostatic potential maps for these two events, the dawn cell extension appears more prominent in the event occurring on March 26, 2008. This is consistent with the DMSP Special Sensor Ultraviolet Spectrographic Imager (SUSSI) Lyman-Birge-Hopfield long (LBHL) data and the results presented by Nishimura et al. (2020) in which the event on March 26, 2008 appears to have a more intense substorm surge than the event occurring on April 5, 2010.

4 Summary of Comparisons between STEVE and non-STEVE Substorm Events

This section provides four tables that summarize the data analysis results presented in Section 3 and compare the key differences identified between STEVE and non-STEVE substorm events. Table 3 explains the morphological and timing differences in the dawn cell extension observed in AMGeO convection maps between STEVE and non STEVE substorm events. In Table 4 comparisons of PCA results are summarized between both categories of events. Magnitude differences in cross-polar cap potential and IMF By and IMF Bz are discussed in Table 5 and Table 6, respectively.

Table 3. Summary of the key differences in the dawn-cell extension observed in STEVE and non-STEVE substorm events

Dawn Cell Extension	
STEVE events	Non-STEVE substorm events
The dawn cell extension typically extends farther into the pre-midnight sector (Sections 3.6-3.7).	The dawn cell extension is mostly not as far extended into the pre-midnight sector, localized around midnight (Sections 3.6-3.7).
Significant dawn-cell extension is present from the growth through recovery phase for 9/10 events (Section 3.6). Typical behaviours among 32 events are the same (Section 3.5).	Significant dawn-cell extension is present from the growth to end of expansion phase for 7/10 events (Section 3.6). Typical behaviours among 32 events are the same (Section 3.5).

5 Discussion

In Table 1 in Section 2.1 the STEVE optical onset time in UT for the 32 STEVE events investigated in this study are defined. It should be noted that there are some ambiguities associated with the definition of these STEVE onset times. As reported by (GallardoLacourt et al., 2018), the STEVE optical onset is defined as the time when STEVE is first observed within the field-of-view of a ground-based auroral imager. Since STEVE is a westward moving structure, it is possible that STEVE forms further eastward resulting in a time difference between the initial appearance of STEVE and its detection by an ASI. Nevertheless, STEVE propagates rapidly westward potentially, so discrepancies may be on the order of minutes. This study also utilizes the substorm onset times obtained from the SuperMAG substorm database for the 32 non-STEVE substorm events investigated (Table 2). The substorm onset times in the SuperMAG dataset are defined using the technique presented in Newell and Gjerloev (2011). There are different definitions of substorm onset timing depending on the technique or method used for substorm onset identification (e.g., Frey et al. (2004); Nishimura et al. (2010); Forsyth et al. (2015)).

Regarding the physical implications of the Harang Reversal, previous studies on ionospheric convection patterns [e.g., Grocott et al. (2010); Kamide and Kokubun (1996); Zou et al. (2009)] have shown a relationship between the dawn-dusk asymmetry in the electrostatic potential, substorms, and the formation of the Harang discontinuity or Harang reversal. Specifically, Grocott et al. (2010) reported that the IMF strongly governs the behaviour of this asymmetry during the substorm growth phase; however, this asymmetry was not maintained around magnetic midnight during the expansion phase. This result is consistent with our analysis of 32 substorm events without the presence of STEVE. By contrast, for the 32 STEVE events the asymmetric nature of the electrostatic potential pattern is strong even during the recovery phase, after STEVE is optically observed. As reported by GallardoLacourt et al. (2018), the STEVE events analyzed here do not exhibit an IMF dependence.

In addition, this asymmetry has been known to be associated with the formation of the Harang reversal. Harang (1946) originally named it *Harang discontinuity* based on the ground-based magnetometer observations showing the directional change in magnetic field perturbations in the region. The Harang reversal thus corresponds to the location where the eastward electrojet overlaps with the westward electrojet and represents a region of converging electric fields in the nightside ionosphere at auroral latitudes. More broadly, the Harang reversal can be considered in terms of a convection structure where the two auroral electrojets overlap. This study adopts the Harang reversal definition in terms of ionospheric convection structure features, similarly to Ohtani et al. (2016), instead of its original definition based on ground magnetic disturbances. Some physical insights into this high-latitude ionospheric convection structure can be gained from the work by Gkioulidou et al. (2009). They have investigated electrodynamics involved in the Harang reversal's formation and reported that the equatorward portion of the convergent electric fields (associated with the Harang reversal) contribute to intensify the initial poleward electric field in that region, producing strong westward subauroral $\mathbf{E} \times \mathbf{B}$ drifts identified as SAPS. As previously mentioned, this study reveals that the asymmetric electrostatic potential patterns observed for regular substorms in absence of STEVE is mainly observed during the growth and expansion phase of substorm. In contrast, for the STEVE events studied in this paper, the asymmetric mode of variability starts to form during the substorm growth phase and is maintained well into the recovery phase beyond STEVE optical onset. Considering the results reported by Gkioulidou et al. (2009), this study's results suggest that the Harang reversal is present for a longer time during STEVE events than regular substorms, potentially playing a role in enhancing even further westward subauroral $\mathbf{E} \times \mathbf{B}$ drifts. This mechanism could help explain the connection between STEVE and extreme SAIDs previously reported in Archer et al. (2019a); MacDonald et al. (2018).

Furthermore, a recent study by Nishimura et al. (2020) has reported on the magnetospheric conditions for two STEVE events and compared to conditions found during two non-STEVE SAID/SAPS substorm events. Using SUSSI images from DMSP satellites, they have found that for STEVE events the substorm surge and intense upward field-aligned currents, reaching into the pre-midnight dusk sector, but for non-STEVE substorms they are localized around midnight. Although more research is needed to clearly elucidate this, the electrostatic potential asymmetry identified in this study could help explain the surge's fast motion reported by Nishimura et al. (2020). The two STEVE events included in the Nishimura et al. (2020) investigation are the March 26, 2008 and April 5, 2010 events, which are also investigated in this paper. The dawn-cell extensions seen in the AMGeO convection patterns produced for these events display qualitative similarities to the westward substorm surge extension reported in Nishimura et al. (2020) (see Supplementary Material Movie 1 and Movie 2 for more information). From a comparative visual inspection of the AMGeO convection patterns for the STEVE events occurring on March 26, 2008 and April 5, 2010, the westward extension of the dawn cell appears more prominent for the event occurring on March 26, 2008. This is in agreement with the DMSP's SUSSI LBHL image analysis presented by Nishimura et al. (2020). Physical implications of the potential connection between the dawn-cell extension trend found in AMGeO electrostatic potential maps in this study and the substorm surge identified in SUSSI images in Nishimura et al. (2020) may be further investigated in the future; however, it should be noted that there are differences in terms of the data being used and the scales of interests between these studies.

6 Conclusions

This paper presents the first comprehensive study focusing on characteristic global-scale ionospheric electrodynamics associated with STEVE events and identifies key differences from non-STEVE substorm events. We have found distinguishing differences in the mean convection patterns and global modes of convection patterns variability around the mean for these categories of events. This data-intensive STEVE study involves 192 total hours of 5-minute assimilative mapping analysis by AMGeO. These assimilative mapping analysis of high-latitude ionospheric convection patterns are obtained from a large amount of SuperDARN plasma drift data and ground-based magnetometer data distributed by SuperMAG for 32 STEVE and 32 non-STEVE substorm events. The PCA, superposed epoch analysis, and correlation analysis are further applied to the AMGeO maps to identify key differences between STEVE and non-STEVE substorm events as summarized in Section 4. In general, our findings are consistent with the previous studies by GallardoLacourt et al. (2018) and Nishimura et al. (2020) suggesting that STEVE optical events occur during specific and unique types of substorms that are distinct from typical substorms where STEVE is not present.

Main findings regarding specific differences in the global convection patterns observed during substorms with and without STEVE events are categorized into four main categories including magnitude, morphology, and timing as well as the relationship to geomagnetic activity parameters described below.

Magnitude

- A magnitude difference in cross-polar cap potential drop observed in the mean electrostatic potential maps for STEVE and non-STEVE substorm events is about 10 kV. For STEVE events the magnitude is 48.15 kV compared to non-STEVE substorm events at 39.32 kV (Section 3.2).
- A larger magnitude of cross-polar cap potential is present across the entire 3-hr duration of the superposed epoch analysis for STEVE events compared to non-STEVE substorm events (Sections 3.3 and 3.4).

Morphology

- There is also a difference in the dawn-cell extension morphology between STEVE and non-STEVE substorm events. For the majority of the 32 STEVE events investigated in this study, a strong westward extension of the dawn cell, penetrating into the dusk cell in the pre-midnight sector near subauroral latitudes, is observed (Section 3.1).
- A dawn cell extension is also observed in the AMGeO electrostatic potential maps of non-STEVE substorm events; however, the dawn cell morphology is typically not as far extended into the pre-midnight sector and is more localized around midnight (Section 3.4).
- The spatial morphology of the dawn-cell extension mode (PC3) for STEVE events is significantly more pronounced and farther extending into the pre-midnight sector than PC3 for non-STEVE substorm events (Figure 5, Figure 8). There is a direct relationship observed between the maximum of PC3 coefficients and the extent of the dawn-cell extension in terms of magnitude and penetration depth into the dusk cell for both categories of events. Due to the spatial morphology differences in PC3, the dawn-cell extension observed at the maximum of PC3 coefficients for STEVE events tends to be more intense than that observed for non-STEVE substorm events (Figure 11).

Timing

- Although there is variability among individual events, typically during STEVE events the dawn cell extension starts during the growth phase of substorm, persisting all the way through the recovery phase of substorm (Section 3.6). Non-STEVE substorm events also have variations among individual events, but for the majority of events the dawn cell extension is visually detected during the growth phase through the end of the expansion phase of substorm (Section 3.6).
- There are also several notable differences that have been identified related to the timing in PC coefficients variation over the duration of STEVE and non-STEVE substorm events (Section 4 Table 4). For STEVE events, the median of PC1 coefficients continues to increase during the substorm recovery phase as opposed to approaching zero as observed for non-STEVE substorms (Figure 11). This difference in the evolution of PC1 coefficients is related to the prolonged dawn-dusk asymmetry observed for STEVE events.

Relationship to Geomagnetic Activity Parameters

- Although further investigation is required to understand physical connections between IMF and modes of variability of global convection patterns, notable differences have been observed in IMF By and IMF Bz between STEVE and non-STEVE substorm events. The dawn-cell extension associated with STEVE events is found largely unrelated to IMF By, which is in agreement with the past studies. While the median of IMF By is mostly negative for the 3 hour duration of superposed epoch analysis for STEVE events (Figure 6 (e)), for non-STEVE substorms, IMF By is mostly positive (Figure 9 (e)). The temporal variation of the median of IMF Bz, reaching to the greatest negative value at substorm onset, is generally similar between these two category of events, but the variation is more distinct for non-STEVE substorms (Figures 6 (h) and 9 (h)).
- The greatest minimum magnitude of the AL-index for STEVE events is -614 nT and the minimum AL-index for non-STEVE substorm events is found to be -519 nT (2.1). This result is consistent with the GallardoLacourt et al. (2018) work wherein larger AL values and a long-lasting expansion phase have been found to be associated with STEVE events. Although the mean magnitude of AL index is about 100 nT stronger for the STEVE events analyzed in this study, there is no clear indication that the strength of AL could be used to predict the likelihood of observing a stronger (or weaker) dawn-cell extension. As an example of this, the event study reported by

Nishimura et al. (2020) and presented as a case study in Section 3.7 shows one of the most pronounced dawn-cell westward extension, but it is not among the events with greatest AL minimum magnitudes.

In summary, the global modes of high-latitude ionospheric electrodynamics associated with optical STEVE events characterized in this study provide an important clue to better understand what makes STEVE events different from other substorms, and helps to further unravel physical mechanisms behind these STEVE events. In addition, this investigation showcases the exceptional capabilities of AMGeO software when utilized as a data-mining research tool for uncovering unknown physical characteristics of high-latitude electrodynamics from large amounts of geospace data sets. Our future work with AMGeO includes analyzing different features of high-latitude electrodynamics during SAPS and SAID events by using previously analyzed events [e.g., Archer et al. (2019a); Erickson et al. (2011)]; such study could help us understand the global ionospheric conditions that give rise to the extreme SAID parameters detected during STEVE events.

Acknowledgments

We are grateful and would like to show appreciation to Elizabeth MacDonald for her support on the STEVE research and help with citizen science data at the initial stage of the study. We would also like to extend a special thanks and appreciation to the Boulder Solar Alliance REU program and Martin Snow. VS would like to thank Starr Svaldi for supporting her and for her proofreading expertise. This study is mainly supported by the National Science Foundation (NSF) ICER 1928403 and AGS 1848544 awards to the University of Colorado Boulder. BGL is supported by a NASA Postdoctoral Program (NPP) fellowship at NASA GSFC, administered by Oak Ridge Associated Universities (ORAU) under contract with NASA. AMGeO open source software is available from <https://amgeo.colorado.edu/> upon registration. AMGeO is supported by the NSF EarthCube awards ICER 1928403, ICER 1928327, and ICER 1928358. We acknowledge the use of SuperDARN data (<http://vt.superdarn.org/tiki-index.php>). SuperDARN is a collection of radars funded by national scientific funding agencies of Australia, Canada, China, France, Italy, Japan, Norway, South Africa, United Kingdom and the United States of America. We acknowledge the use of the substorm timing list identified by the Newell and Gjerloev technique (Newell and Gjerloev, 2011), the SMU and SML indices (Newell and Gjerloev, 2011), magnetometer data distributed by the SuperMAG collaboration (<https://supermag.jhuapl.edu>, Gjerloev et al. 2012). For the ground magnetometer data we acknowledge: INTERMAGNET, Alan Thomson; CARISMA, PI Ian Mann; CANMOS, Geomagnetism Unit of the Geological Survey of Canada; The S-RAMP Database, PI K. Yumoto and Dr. K. Shiokawa; The SPIDR database; AARI, PI Oleg Troshichev; The MACCS program, PI M. Engebretson; GIMA; MEASURE, UCLA IGPP and Florida Institute of Technology; SAMBA, PI Eftyhia Zesta; 210 Chain, PI K. Yumoto; SAMNET, PI Farideh Honary; IMAGE, PI Liisa Juusola; Finnish Meteorological Institute, PI Liisa Juusola; Sodankyl Geophysical Observatory, PI Tero Raita; UiT the Arctic University of Norway, Troms Geophysical Observatory, PI Ragnar G. Johnsen; GFZ German Research Centre For Geosciences, PI Jrgen Matzka; Institute of Geophysics, Polish Academy of Sciences, PI Anne Neska and Jan Reda; Polar Geophysical Institute, PI Alexander Yahnin and Yaroslav Sakharov; Geological Survey of Sweden, PI Gerhard Schwarz; Swedish Institute of Space Physics, PI Masatoshi Yamauchi; AUTUMN, PI Martin Connors; DTU Space, Thom Edwards and PI Anna Willer; South Pole and McMurdo Magnetometer, PI's Louis J. Lanzarotti and Alan T. Weatherwax; ICESTAR; RAPIDMAG; British Antarctic Survey; MacMac, PI Dr. Peter Chi; BGS, PI Dr. Susan Macmillan; Pushkov Institute of Terrestrial Magnetism, Ionosphere and Radio Wave Propagation (IZMIRAN); MFGI, PI B. Heilig; Institute of Geophysics, Polish Academy of Sciences, PI Anne Neska and Jan Reda; University of LAquila, PI M. Vellante; BCMT, V. Lesur and A. Chambodut; Data obtained in cooperation with Geoscience Australia, PI Andrew Lewis; AALPIP, co-PIs Bob Clauer and Michael Hartinger; SuperMAG, PI Jesper W. Gjerloev; Data obtained in cooperation with the Australian Bureau of Meteorology, PI

Richard Marshall. The OMNI data were obtained from the GSFC/SPDF OMNIWeb interface and can be acquired at <https://omniweb.gsfc.nasa.gov> The Redline Emission Geospace Observatory (REGO) is a joint Canada Foundation for Innovation and Canadian Space Agency project developed by the University of Calgary. THEMIS and REGO ASI data can be obtained from <http://data.phys.ucalgary.ca>. The Swarm satellite A and C data is used from the level 1b calibrated, validated instrument data made accessible to the public through the European Space Agency (<https://swarm-diss.eo.esa.int>). All AMGeO ionospheric convection patterns used in this study are available at <https://osf.io/26ae5/>.

References

- AMGeO Collaboration. (2019, December). *A Collaborative Data Science Platform for the Geospace Community: Assimilative Mapping of Geospace Observations (AMGeO) v1.0.0* (Tech. Rep.). (Publisher: Zenodo) doi: 10.5281/zenodo.3564914
- Archer, W. E., Gallardo-Lacourt, B., Perry, G. W., St.-Maurice, J. P., Buchert, S. C., & Donovan, E. (2019a). Steve: The optical signature of intense subauroral ion drifts. *Geophysical Research Letters*, *46*(12), 6279–6286. Retrieved from <https://agupubs.onlinelibrary.wiley.com/doi/abs/10.1029/2019GL082687> doi: <https://doi.org/10.1029/2019GL082687>
- Archer, W. E., Maurice, J.-P. S., GallardoLacourt, B., Perry, G. W., Cully, C. M., Donovan, E., ... Eurich, D. (2019b). The Vertical Distribution of the Optical Emissions of a Steve and Picket Fence Event. *Geophysical Research Letters*, *46*(19), 10719–10725. Retrieved 2021-03-02, from <https://agupubs.onlinelibrary.wiley.com/doi/abs/10.1029/2019GL084473> (eprint: <https://agupubs.onlinelibrary.wiley.com/doi/pdf/10.1029/2019GL084473>) doi: <https://doi.org/10.1029/2019GL084473>
- Chisham, G., Lester, M., Milan, S. E., Freeman, M. P., Bristow, W. A., Grocott, A., ... Walker, A. D. M. (2007, January). A decade of the Super Dual Auroral Radar Network (SuperDARN): scientific achievements, new techniques and future directions. *Surveys in Geophysics*, *28*(1), 33–109. Retrieved 2021-03-02, from <https://doi.org/10.1007/s10712-007-9017-8> doi: 10.1007/s10712-007-9017-8
- Cousins, E. D. P., & Shepherd, S. G. (2010). A dynamical model of high-latitude convection derived from SuperDARN plasma drift measurements. *Journal of Geophysical Research: Space Physics*, *115*(A12). Retrieved 2021-03-04, from <https://agupubs.onlinelibrary.wiley.com/doi/abs/10.1029/2010JA016017> (eprint: <https://agupubs.onlinelibrary.wiley.com/doi/pdf/10.1029/2010JA016017>) doi: <https://doi.org/10.1029/2010JA016017>
- Erickson, P. J., Beroz, F., & Miskin, M. Z. (2011). Statistical characterization of the american sector subauroral polarization stream using incoherent scatter radar. *Journal of Geophysical Research: Space Physics*, *116*(A5). Retrieved from <https://agupubs.onlinelibrary.wiley.com/doi/abs/10.1029/2010JA015738> doi: <https://doi.org/10.1029/2010JA015738>
- Forsyth, C., Rae, I. J., Coxon, J. C., Freeman, M. P., Jackman, C. M., Gjerloev, J., & Fazakerley, A. N. (2015). A new technique for determining substorm onsets and phases from indices of the electrojet (sophie). *Journal of Geophysical Research: Space Physics*, *120*(12), 10,592–10,606. Retrieved from <https://agupubs.onlinelibrary.wiley.com/doi/abs/10.1002/2015JA021343> doi: <https://doi.org/10.1002/2015JA021343>
- Frey, H. U., Mende, S. B., Angelopoulos, V., & Donovan, E. F. (2004). Substorm onset observations by image-fuv. *Journal of Geophysical Research: Space Physics*, *109*(A10). Retrieved from <https://agupubs.onlinelibrary.wiley.com/doi/abs/10.1029/2004JA010607> doi: <https://doi.org/10.1029/2004JA010607>
- Gallardo-Lacourt, B., Perry, G. W., Archer, W. E., & Donovan, E. (2019). *How Did We Miss This? An Upper Atmospheric Discovery Named STEVE* (No. 100). Retrieved 2021-03-17, from <https://eos.org/features/how-did-we-miss-this-an>

- upper-atmospheric-discovery-named-steve doi: <https://doi.org/10.1029/2019EO117351>
- GallardoLacourt, B., Nishimura, Y., Donovan, E., Gillies, D. M., Perry, G. W., Archer, W. E., ... Spanswick, E. L. (2018). A Statistical Analysis of STEVE. *Journal of Geophysical Research: Space Physics*, 123(11), 9893–9905. Retrieved 2021-02-28, from <https://agupubs.onlinelibrary.wiley.com/doi/abs/10.1029/2018JA025368> (eprint: <https://agupubs.onlinelibrary.wiley.com/doi/pdf/10.1029/2018JA025368>) doi: <https://doi.org/10.1029/2018JA025368>
- Gillies, D. M., Donovan, E., Hampton, D., Liang, J., Connors, M., Nishimura, Y., ... Spanswick, E. (2019). First Observations From the TREx Spectrograph: The Optical Spectrum of STEVE and the Picket Fence Phenomena. *Geophysical Research Letters*, 46(13), 7207–7213. Retrieved 2021-03-12, from <https://agupubs.onlinelibrary.wiley.com/doi/abs/10.1029/2019GL083272> (eprint: <https://agupubs.onlinelibrary.wiley.com/doi/pdf/10.1029/2019GL083272>) doi: <https://doi.org/10.1029/2019GL083272>
- Gjerloev, J. W. (2012). The SuperMAG data processing technique. *Journal of Geophysical Research: Space Physics*, 117(A9). Retrieved 2021-03-04, from <https://agupubs.onlinelibrary.wiley.com/doi/abs/10.1029/2012JA017683> (eprint: <https://agupubs.onlinelibrary.wiley.com/doi/pdf/10.1029/2012JA017683>) doi: <https://doi.org/10.1029/2012JA017683>
- Gkioulidou, M., Wang, C.-P., Lyons, L. R., & Wolf, R. A. (2009). Formation of the harang reversal and its dependence on plasma sheet conditions: Rice convection model simulations. *Journal of Geophysical Research: Space Physics*, 114(A7). Retrieved from <https://agupubs.onlinelibrary.wiley.com/doi/abs/10.1029/2008JA013955> doi: <https://doi.org/10.1029/2008JA013955>
- Grocott, A., Milan, S. E., Yeoman, T. K., Sato, N., Yukimatu, A. S., & Wild, J. A. (2010). Superposed epoch analysis of the ionospheric convection evolution during substorms: IMF BY dependence. *Journal of Geophysical Research: Space Physics*, 115(A5). Retrieved 2021-03-11, from <https://agupubs.onlinelibrary.wiley.com/doi/abs/10.1029/2010JA015728> (eprint: <https://agupubs.onlinelibrary.wiley.com/doi/pdf/10.1029/2010JA015728>) doi: <https://doi.org/10.1029/2010JA015728>
- Harang, L. (1946). The mean field of disturbance of polar geomagnetic storms. *Terrestrial Magnetism and Atmospheric Electricity*, 51(3), 353–380. Retrieved from <https://agupubs.onlinelibrary.wiley.com/doi/abs/10.1029/TE051i003p00353> doi: <https://doi.org/10.1029/TE051i003p00353>
- Harding, B. J., Mende, S. B., Triplett, C. C., & Wu, Y.-J. J. (2020). A Mechanism for the STEVE Continuum Emission. *Geophysical Research Letters*, 47(7), e2020GL087102. Retrieved 2021-03-12, from <https://agupubs.onlinelibrary.wiley.com/doi/abs/10.1029/2020GL087102> (eprint: <https://agupubs.onlinelibrary.wiley.com/doi/pdf/10.1029/2020GL087102>) doi: <https://doi.org/10.1029/2020GL087102>
- Kamide, Y., & Kokubun, S. (1996). Two-component auroral electrojet: Importance for substorm studies. *Journal of Geophysical Research: Space Physics*, 101(A6), 13027–13046. Retrieved from <https://agupubs.onlinelibrary.wiley.com/doi/abs/10.1029/96JA00142> doi: <https://doi.org/10.1029/96JA00142>
- Kivelson, M. G., & Russell, C. T. (1995). *Introduction to space physics*. CCambridge University Press. doi: <https://doi.org/10.1017/9781139878296>
- Liang, J., Shen, Y., Knudsen, D., Spanswick, E., Burchill, J., & Donovan, E. (2019). e-POP and Red Line Optical Observations of Alfvénic Auroras. *Journal of Geophysical Research: Space Physics*, 124(6), 4672–4696. Retrieved 2021-03-12, from <https://agupubs.onlinelibrary.wiley.com/doi/abs/10.1029/2019JA026679> (eprint: <https://agupubs.onlinelibrary.wiley.com/doi/pdf/10.1029/2019JA026679>) doi: <https://doi.org/10.1029/2019JA026679>
- MacDonald, E. A., Donovan, E., Nishimura, Y., Case, N. A., Gillies, D. M., Gallardo-

- Lacourt, B., ... Schofield, I. (2018, March). New science in plain sight: Citizen scientists lead to the discovery of optical structure in the upper atmosphere. *Science Advances*, 4(3), eaaq0030. Retrieved 2021-03-04, from <https://advances.sciencemag.org/content/4/3/eaaq0030> (Publisher: American Association for the Advancement of Science Section: Research Article) doi: 10.1126/sciadv.aaq0030
- Matsuo, T. (2020). Recent Progress on Inverse and Data Assimilation Procedure for High-Latitude Ionospheric Electrodynamics. In M. W. Dunlop & H. Lhr (Eds.), *Ionospheric Multi-Spacecraft Analysis Tools: Approaches for Deriving Ionospheric Parameters* (pp. 219–232). Cham: Springer International Publishing. Retrieved 2021-03-02, from https://doi.org/10.1007/978-3-030-26732-2_10 doi: 10.1007/978-3-030-26732-2_10
- McGranaghan, R., Knipp, D. J., Matsuo, T., & Cousins, E. (2016). Optimal interpolation analysis of high-latitude ionospheric Hall and Pedersen conductivities: Application to assimilative ionospheric electrodynamics reconstruction. *Journal of Geophysical Research: Space Physics*, 121(5), 4898–4923. Retrieved 2021-03-02, from <https://agupubs.onlinelibrary.wiley.com/doi/abs/10.1002/2016JA022486> (eprint: <https://agupubs.onlinelibrary.wiley.com/doi/pdf/10.1002/2016JA022486>) doi: <https://doi.org/10.1002/2016JA022486>
- McGranaghan, R., Knipp, D. J., Matsuo, T., Godinez, H., Redmon, R. J., Solomon, S. C., & Morley, S. K. (2015, December). Modes of high-latitude auroral conductance variability derived from DMSP energetic electron precipitation observations: Empirical orthogonal function analysis: PRIMARY MODES OF CONDUCTANCE VARIABILITY. *Journal of Geophysical Research: Space Physics*, 120(12), 11,013–11,031. Retrieved 2021-03-02, from <http://doi.wiley.com/10.1002/2015JA021828> doi: 10.1002/2015JA021828
- Newell, P. T., & Gjerloev, J. W. (2011). Evaluation of SuperMAG auroral electrojet indices as indicators of substorms and auroral power. *Journal of Geophysical Research: Space Physics*, 116(A12). Retrieved 2021-03-02, from <https://agupubs.onlinelibrary.wiley.com/doi/abs/10.1029/2011JA016779> (eprint: <https://agupubs.onlinelibrary.wiley.com/doi/pdf/10.1029/2011JA016779>) doi: <https://doi.org/10.1029/2011JA016779>
- Newell, P. T., Sotirelis, T., & Wing, S. (2009). Diffuse, monoenergetic, and broadband aurora: The global precipitation budget. *Journal of Geophysical Research: Space Physics*, 114(A9). Retrieved 2021-03-11, from <https://agupubs.onlinelibrary.wiley.com/doi/abs/10.1029/2009JA014326> (eprint: <https://agupubs.onlinelibrary.wiley.com/doi/pdf/10.1029/2009JA014326>) doi: <https://doi.org/10.1029/2009JA014326>
- Nishimura, Y., GallardoLacourt, B., Zou, Y., Mishin, E., Knudsen, D. J., Donovan, E. F., ... Raybell, R. (2019). Magnetospheric Signatures of STEVE: Implications for the Magnetospheric Energy Source and Interhemispheric Conjugacy. *Geophysical Research Letters*, 46(11), 5637–5644. Retrieved 2021-03-11, from <https://agupubs.onlinelibrary.wiley.com/doi/abs/10.1029/2019GL082460> (eprint: <https://agupubs.onlinelibrary.wiley.com/doi/pdf/10.1029/2019GL082460>) doi: <https://doi.org/10.1029/2019GL082460>
- Nishimura, Y., Lyons, L., Zou, S., Angelopoulos, V., & Mende, S. (2010). Substorm triggering by new plasma intrusion: Themis all-sky imager observations. *Journal of Geophysical Research: Space Physics*, 115(A7). Retrieved from <https://agupubs.onlinelibrary.wiley.com/doi/abs/10.1029/2009JA015166> doi: <https://doi.org/10.1029/2009JA015166>
- Nishimura, Y., Yang, J., Weygand, J. M., Wang, W., Kosar, B., Donovan, E. F., ... Nishitani, N. (2020). Magnetospheric Conditions for STEVE and SAID: Particle Injection, Substorm Surge, and Field-Aligned Currents. *Journal of Geophysical Research: Space Physics*, 125(8), e2020JA027782. Retrieved 2021-02-28, from <https://agupubs.onlinelibrary.wiley.com/doi/abs/10.1029/2020JA027782> (eprint: <https://agupubs.onlinelibrary.wiley.com/doi/pdf/10.1029/2020JA027782>)

- doi: <https://doi.org/10.1029/2020JA027782>
- Ohtani, S., Gkioulidou, M., Wang, C.-P., & Wolf, R. A. (2016). The harang reversal and the interchange stability of the magnetotail. *Journal of Geophysical Research: Space Physics*, 121(4), 3278-3292. Retrieved from <https://agupubs.onlinelibrary.wiley.com/doi/abs/10.1002/2015JA022025> doi: <https://doi.org/10.1002/2015JA022025>
- Redmon, R. J., Denig, W. F., Kilcommons, L. M., & Knipp, D. J. (2017). New DMSP database of precipitating auroral electrons and ions. *Journal of Geophysical Research: Space Physics*, 122(8), 9056–9067. Retrieved 2021-03-04, from <https://agupubs.onlinelibrary.wiley.com/doi/abs/10.1002/2016JA023339> (eprint: <https://agupubs.onlinelibrary.wiley.com/doi/pdf/10.1002/2016JA023339>) doi: <https://doi.org/10.1002/2016JA023339>
- Zou, S., Lyons, L. R., Nicolls, M. J., Heinselman, C. J., & Mende, S. B. (2009). Nightside ionospheric electrodynamics associated with substorms: Pfsr and themis asi observations. *Journal of Geophysical Research: Space Physics*, 114(A12). Retrieved from <https://agupubs.onlinelibrary.wiley.com/doi/abs/10.1029/2009JA014259> doi: <https://doi.org/10.1029/2009JA014259>

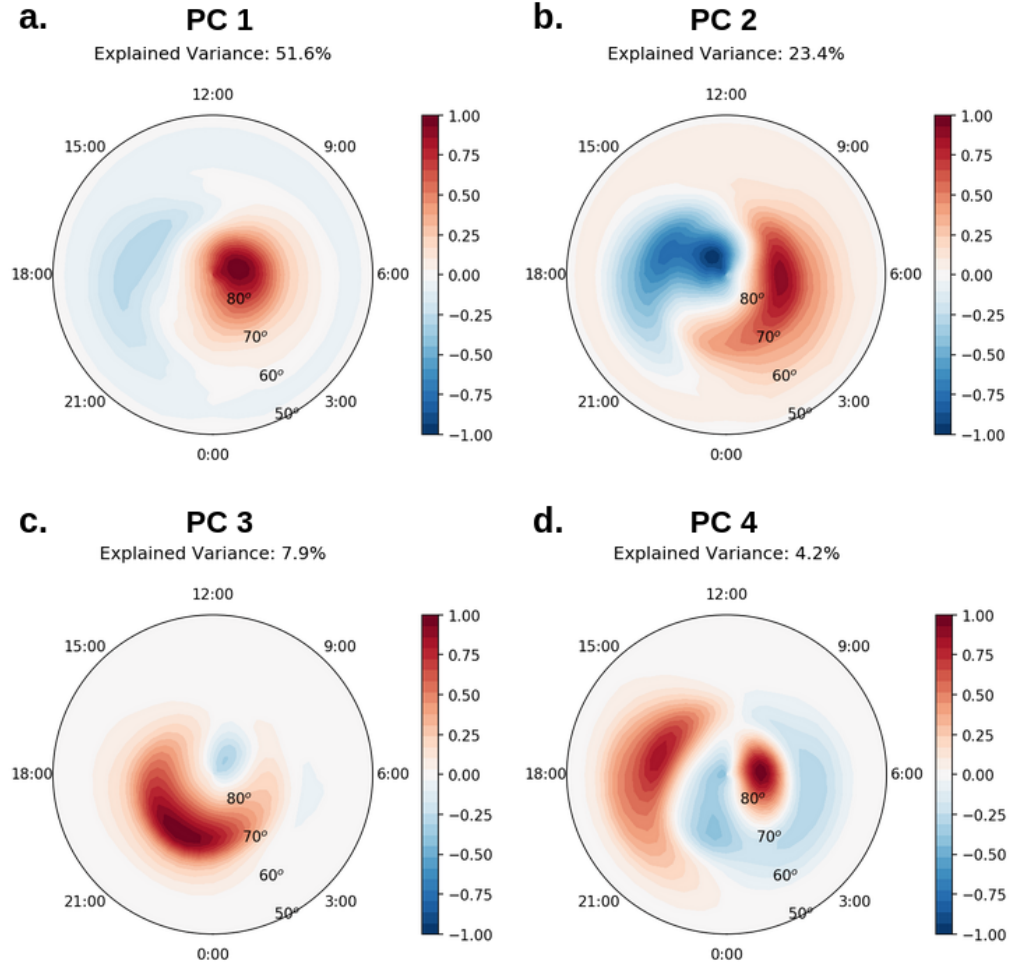


Figure 5. Maps for the first four principal components (PC) of electrostatic potential for 32 STEVE events. The total variance explained by each PC is displayed at the top of each map.

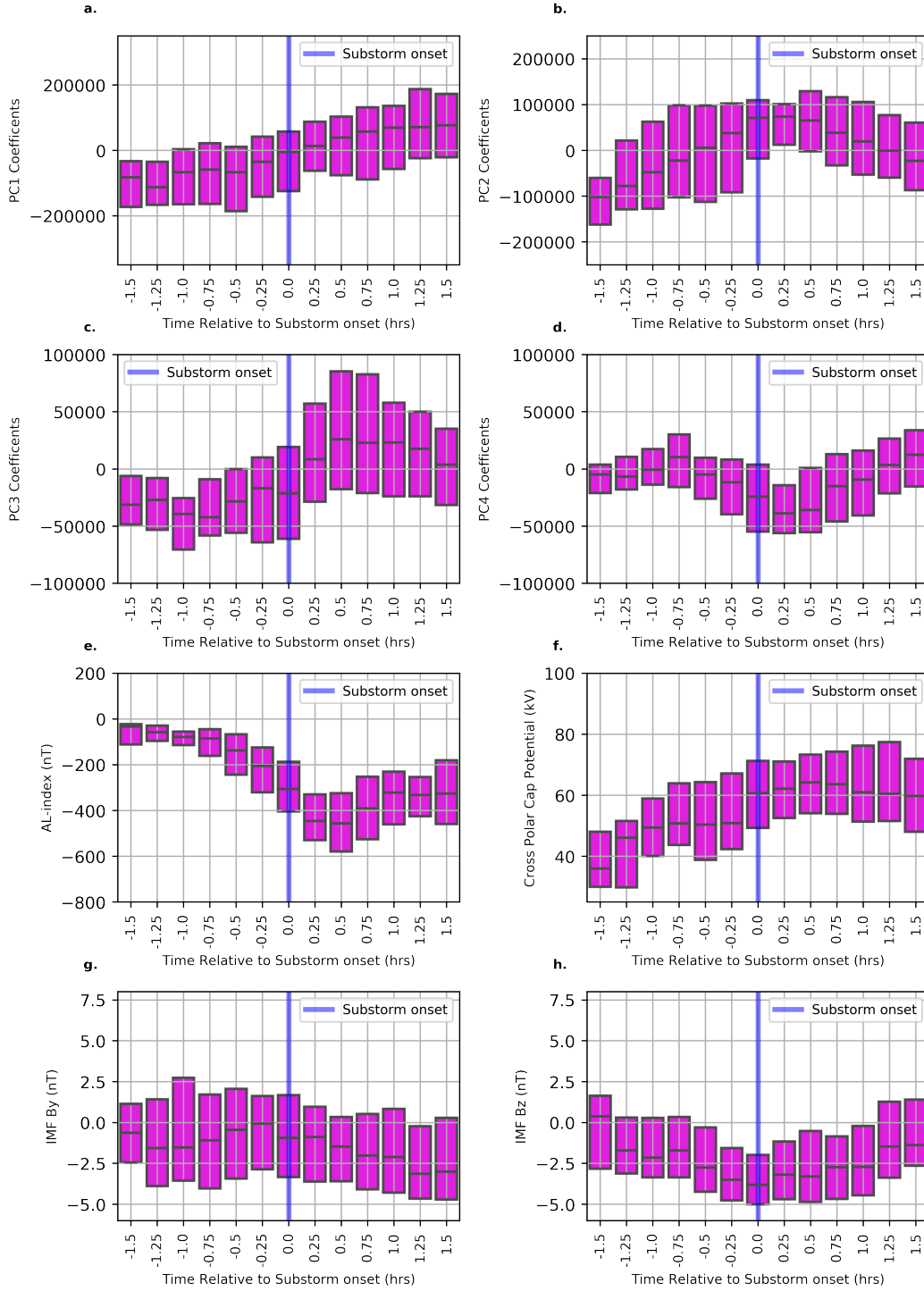


Figure 6. Superposed epoch analysis of PC coefficients for STEVE events displayed over a 3-hour duration centered at substorm onset (1.5 hour prior and 1.5 hour post substorm onset time) for the first four modes (a-d). Superposed epoch analysis for AL-index (e), cross-polar cap potential (f), and IMF By and IMF Bz (g-h) shown in the same manner as for PC coefficients.

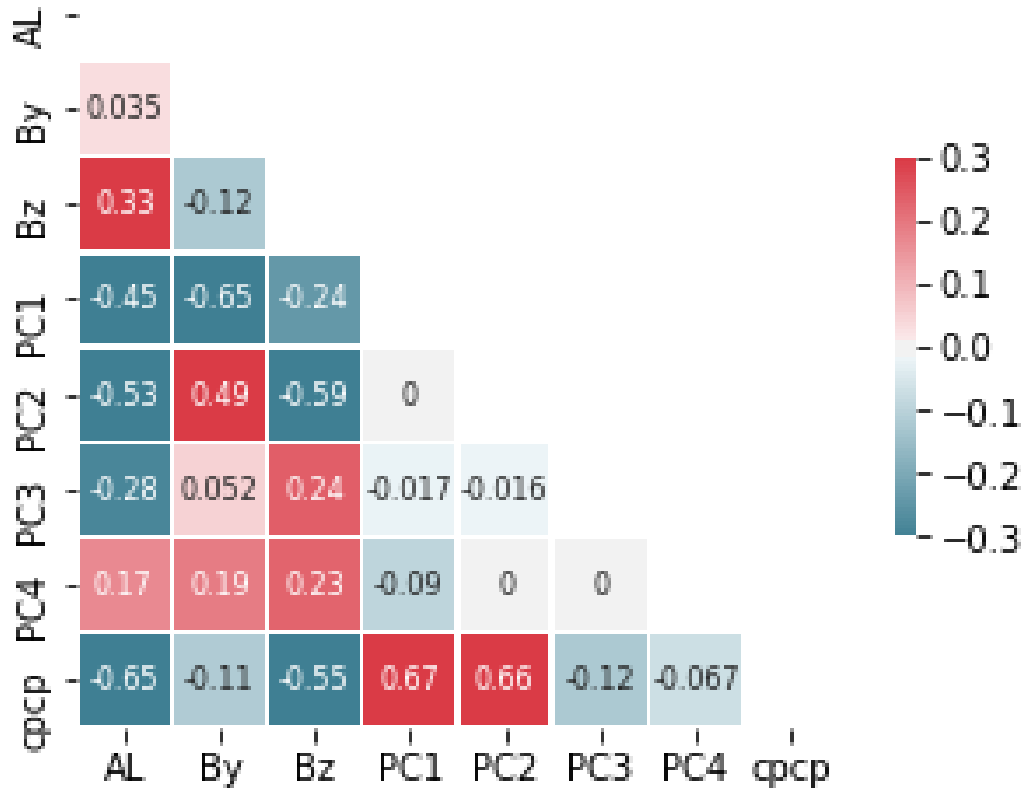


Figure 7. Correlation matrix of PC coefficients, AL-index, AU-index, IMF By, IMF Bz, and cross-polar cap potential for 32 STEVE events.

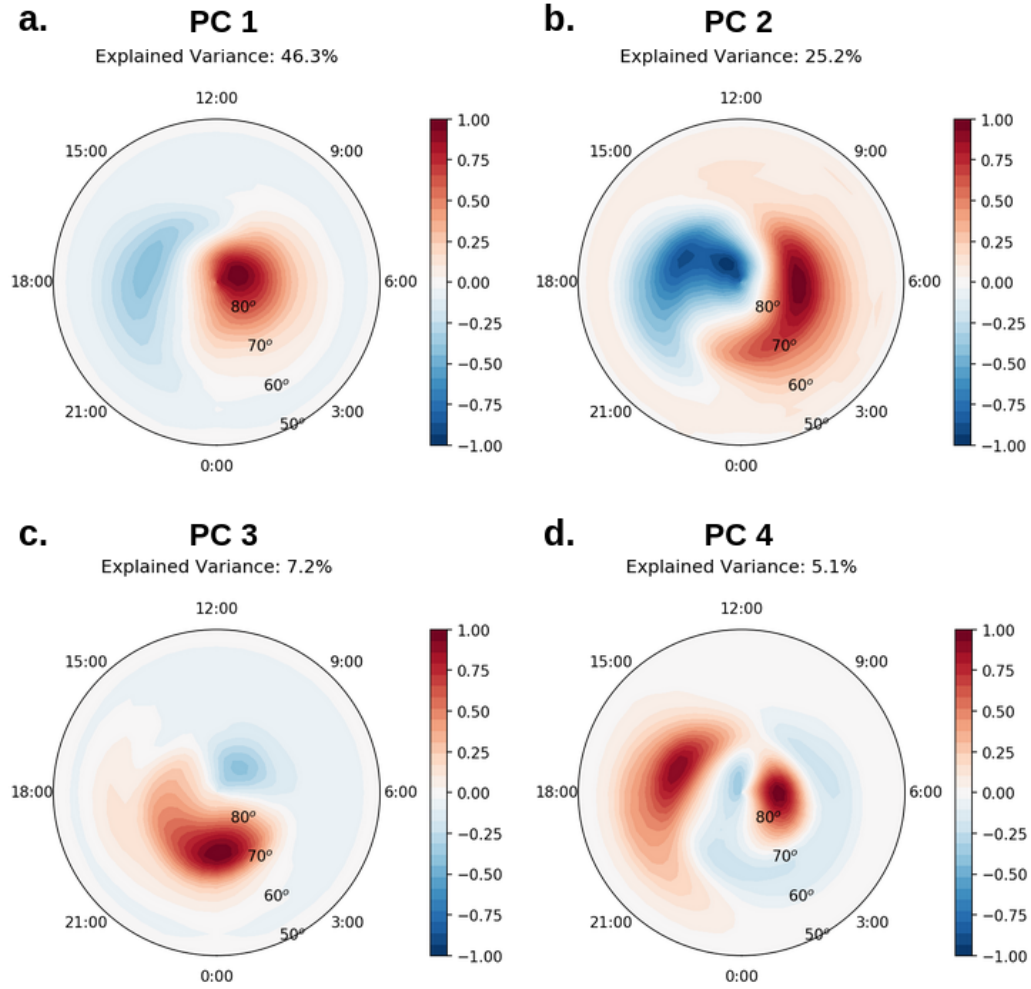


Figure 8. (a.)-(d.) PC maps for the first four principal components of electrostatic potential from 32 non-STEVE substorm events. The explained variance ratio is displayed at the top of each PC plot.

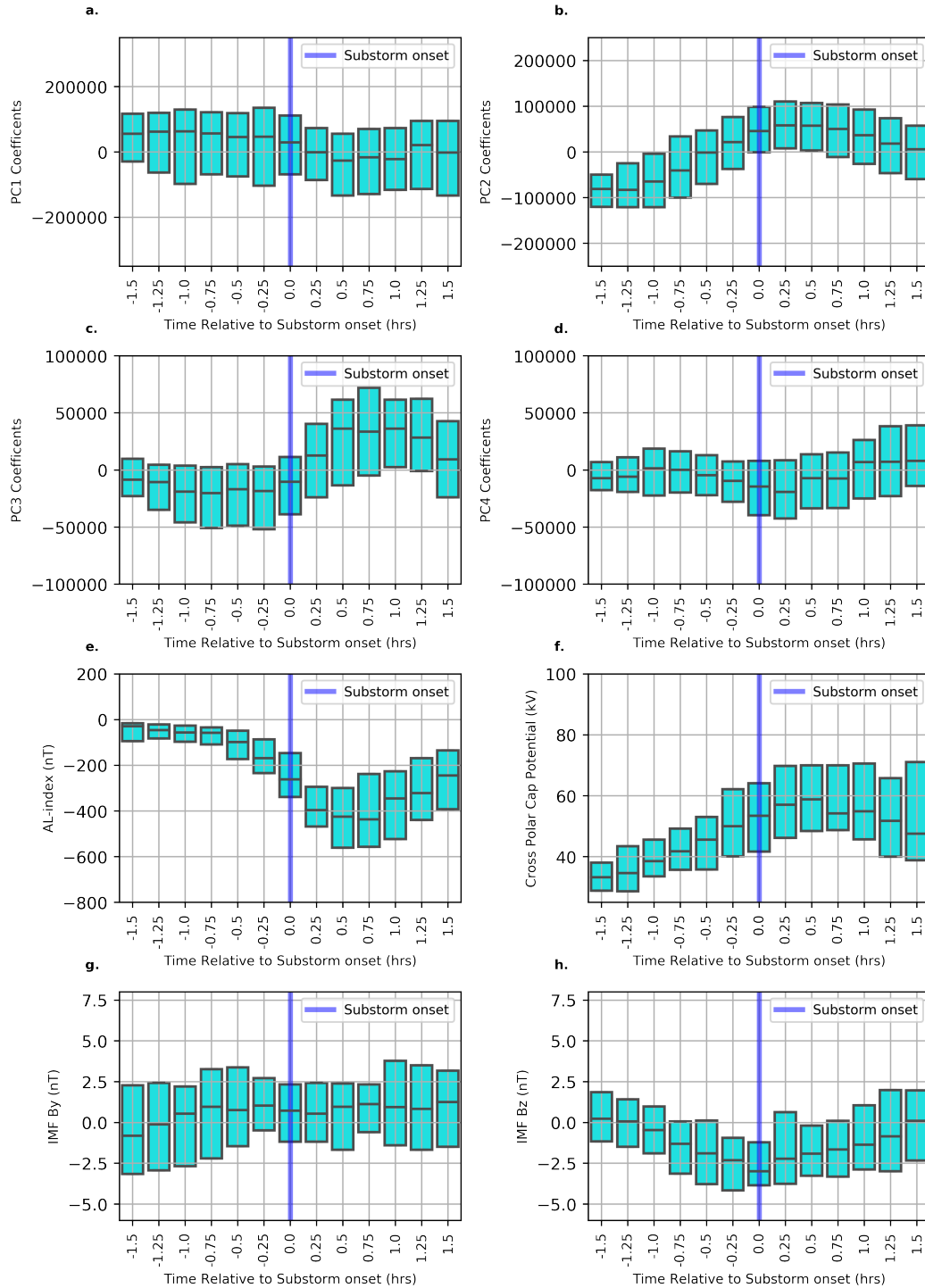


Figure 9. Superposed epoch analysis for non-STEVE substorm events is shown, over a 3-hour duration centered at substorm onset (1.5 hour prior and 1.5 hour post substorm onset time), for PC1-PC4 coefficients (a-d), AL-index (e), cross-polar cap potential (f), and IMF By and Bz (g-h).

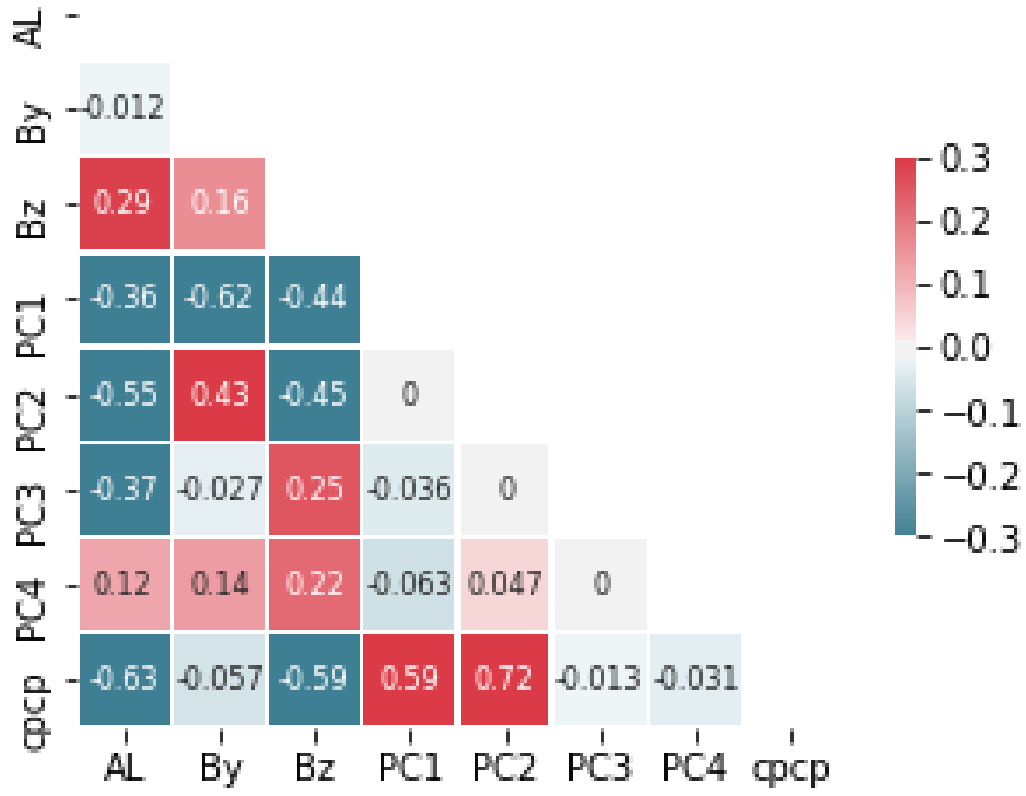


Figure 10. Correlation matrix of PC coefficients, AL-index, AU-index, IMF By and Bz, and cross-polar cap potential for 32 non-STEVE substorm events.

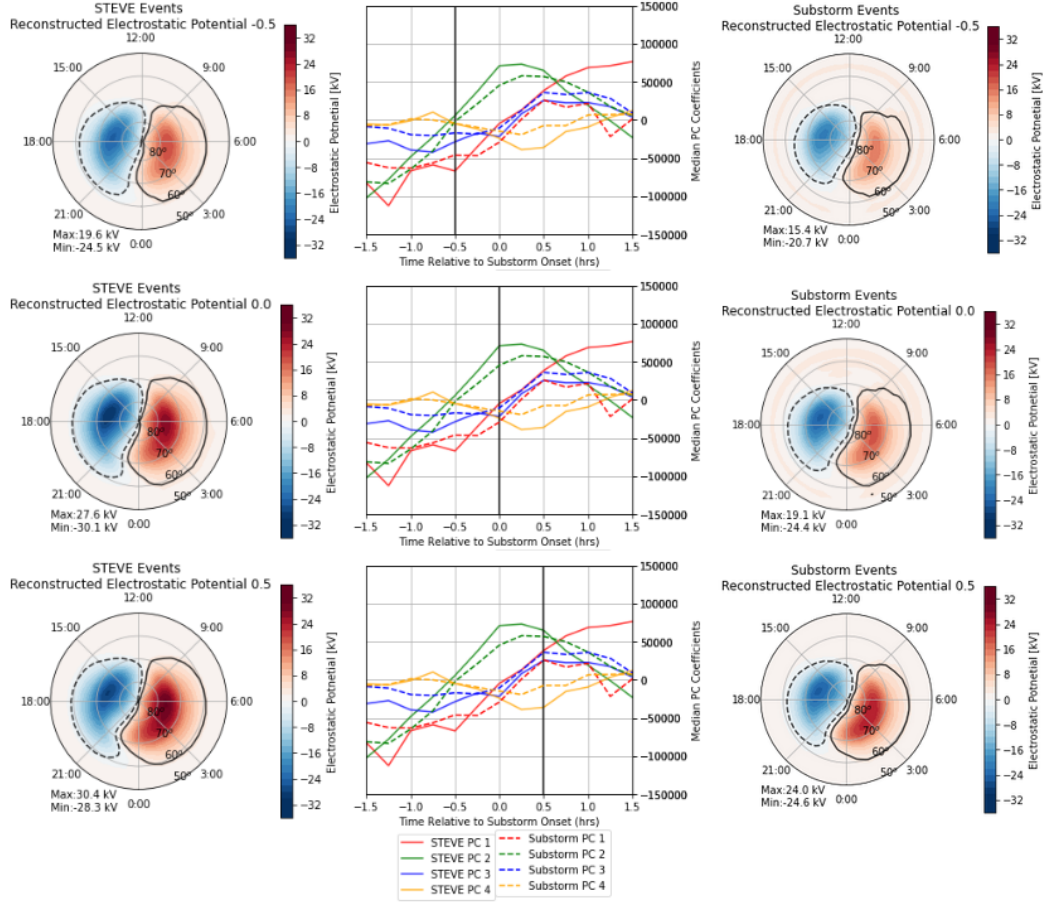


Figure 11. Reconstructed electrostatic potential maps derived for 32 STEVE event (left) and 32 non-STEVE substorm events (right) and time series of median PC coefficients (center). Maps at 0.5 hour prior to substorm onset indicated by a black vertical line in the center plot of median PC coefficients time series (top). Maps at substorm onset (middle) and maps 0.5 hour post substorm onset (bottom) shown in the same format as the maps shown on the top.

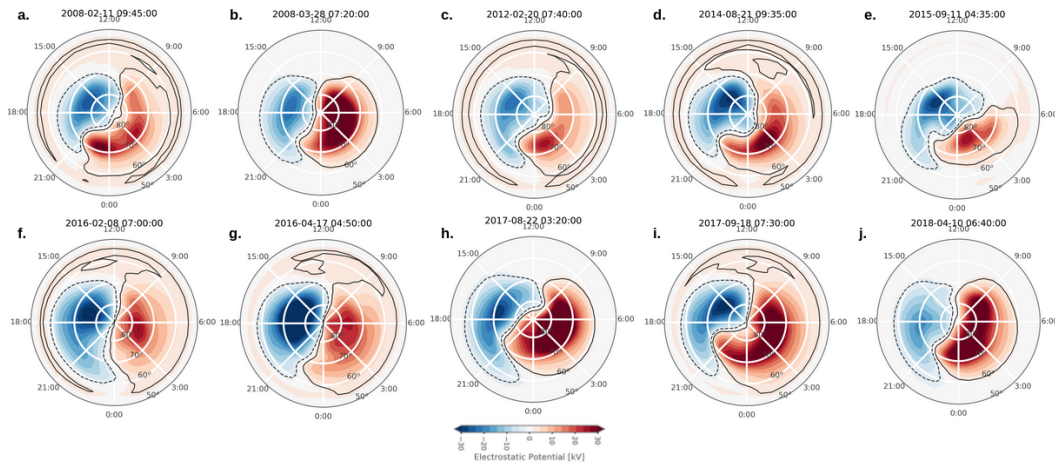


Figure 12. AMGeO electrostatic potential maps displayed at the maximum time of dawn-cell extension mode (PC3) for 10 STEVE events that are selected based on SML minimum values.

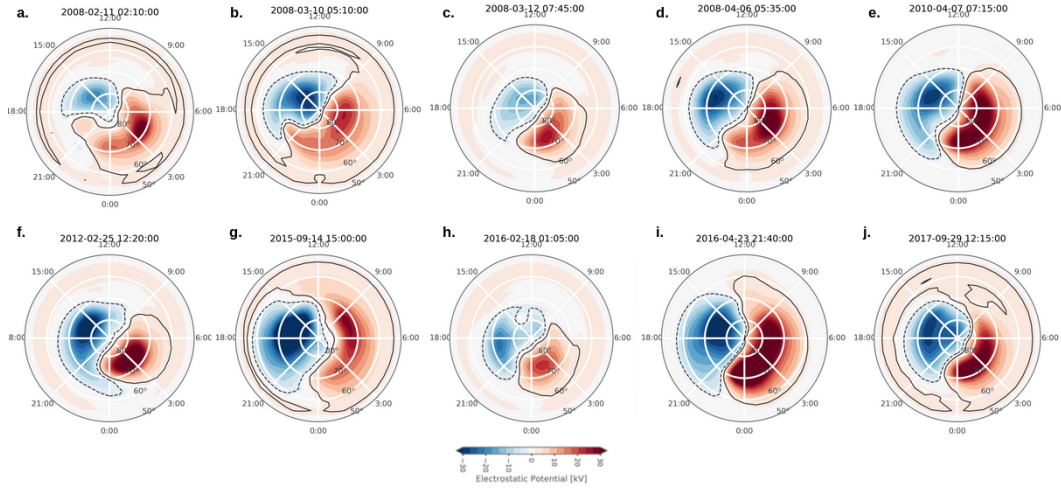


Figure 13. AMGeO electrostatic potential maps displayed at the maximum time of dawn-cell extension mode (PC3) for 10 non-STEVE substorm events that are selected based on SML minimum values.

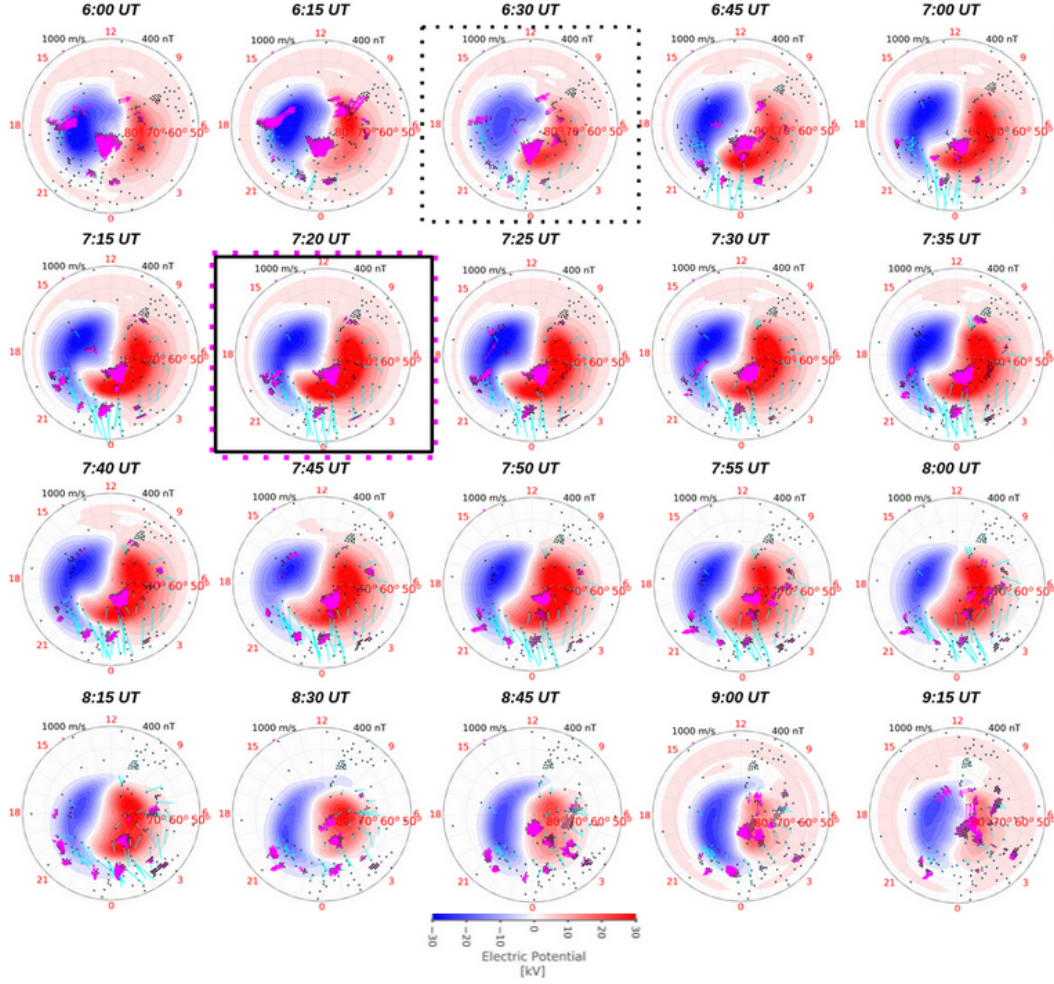


Figure 14. AMGeO electrostatic potential maps for the STEVE event on March 26th 2008 displayed from 6:00 to 9:15 UT. The substorm onset for this STEVE event occurs at 6:00 UT as marked with a black dotted box. The SML minimum is -826 nT at 7:20 UT, which is denoted with a solid black box. The STEVE optical onset occurs at the end of the substorm expansion phase at 7:20 UT as marked by a pink dotted box. SuperDARN plasma drift data (magenta) and SuperMAG ground-level magnetic field data (light blue) are superimposed.

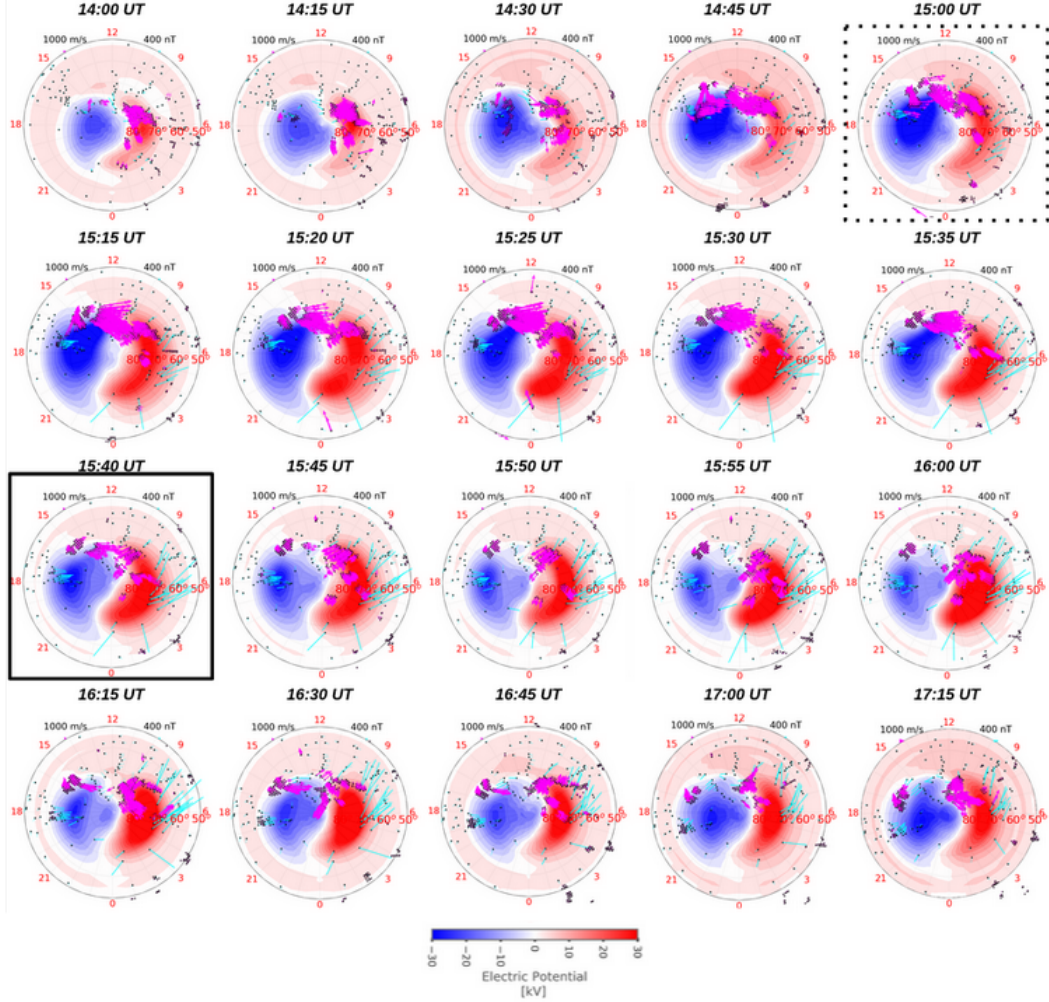


Figure 15. AMGeo electrostatic potential maps for non-STEVE substorm event on September 14, 2015 displayed from 14:00 UT to 17:15 UT. The substorm onset is at 15:00 UT as marked with a black dotted box. The SML minimum is -935 nT at 15:40 UT as denoted by a black solid box. SuperDARN plasma drifts (magenta) and SuperMAG ground-level magnetic field observations (light blue) are superimposed.

Table 4. Summary of the key differences observed in the PCA results for STEVE and non-STEVE substorm events

PC Coefficients and Convection Pattern Behaviors	
STEVE events	Non-STEVE substorm events
<i>PC1 – Dawn-cell intensification mode</i>	
PC1 coefficients do not approach zero for 7/10 events after substorm onset, contributing to prolonged dawn-dusk asymmetry (Section 3.6). The median of PC1 coefficients from 32 events does not approach zero after substorm onset and continues to grow for about 1.25 hours (Section 3.5: Figure 11).	PC1 coefficients tends to approach or reach zero at end of recovery phase for 7/10 events, resulting in the return to a symmetrical two-cell convection pattern (Section 3.6). The median of PC1 coefficients from 32 events approach zero after 1.5 hours post substorm onset (Section 3.5: Figure 11).
PC1 behaviors are related to significant dawn cell extension seen in AMGeO electrostatic potential maps lasting over 1.5 hours post substorm onset in 9/10 events (Section 3.6).	PC1 behaviors are related to some dawn cell extension seen in AMGeO electrostatic potential maps lasting over 1.5 hours post substorm onset in 3/10 events (Section 3.6).
<i>PC2 – Localized nightside dawn-cell penetrating mode</i>	
The peak time of PC2 coefficients vary among 10 individual events, occurring during the expansion phase for 6/10 events and in the recovery phase for 4/10 events (Section 3.6).	The peak time of PC2 coefficients vary considerably among 10 individual events, occurring in the growth phase for 3/10 events, in the expansion phase for 4/10 events, and in the recovery phase for 3/10 events (Section 3.6).
At the peak of PC2, AMGeO electrostatic potential maps show strong dawn-dusk asymmetry on nightside in 10/10 events (Section 3.6).	At the peak of PC2, AMGeO electrostatic potential maps show some dawn-dusk asymmetry on nightside in 10/10 events (Section 3.6).
<i>PC3 – Dawn-cell extension mode</i>	
The dawn-cell extension morphological feature in PC3 is pronounced and extends into the pre-midnight sector (Section 3.3: Figure 5(c)).	The dawn-cell extension morphological feature in PC3 extends less into the pre-midnight sector and is less pronounced (Section 3.4: Figure 8(c)).
PC3 coefficients start to increase prior to substorm onset (Section 3.5: Figure 11, Section 3.6).	PC3 coefficients start to increase after substorm onset (Section 3.5: Figure 11, Section 3.6).
The peak time of PC3 coefficients occurs during the recovery phase for 7/10 events and in the expansion phase for 3/10 events (Section 3.6).	The peak time of PC3 coefficients occurs in the expansion phase for 6/10 events and in the recovery phase for 4/10 events (Section 3.6).
PC3 behaviours are directly related to peaking of dawn-cell extension seen in AMGeO electrostatic potential maps (Section 3.5: Figure 11, Section 3.6, Section 3.7: Figure 14). AMGeO electrostatic potential maps at the time of PC3 peak show strong dawn-cell extension into the pre-midnight sector in 9/10 events (Section 3.6: Figure 12).	PC3 coefficient behaviours are similar to those observed during STEVE events (Section 3.5: Figure 11). Due to the difference in PC3 morphology itself the AMGeO electrostatic potential maps at the time of PC3 peak shows a less pronounced and more diverse appearance of the dawn-cell extension in 10/10 events (Section 3.6: Figure 13).
<i>PC4 – Weak asymmetry mode</i>	
PC4 does not contribute to the key differences due to its small magnitudes.	

Table 5. Summary of the key differences observed in the cross-polar cap potential for STEVE and non-STEVE substorm events

Cross-Polar Cap Potential	
STEVE events	Non-STEVE substorm events
The mean electrostatic potential estimated from all 32 STEVE events is 48.15 kV (Section 3.2: Figure 4 (a)).	The mean electrostatic potential estimated from all 32 non-STEVE substorm events is 39.32 kV (Section 3.2: Figure 4 (b)).
Larger magnitude of cross-polar cap potential across the 3-hour duration of superposed epoch analysis (Section 3.3: Figure 6 (f)).	Weaker magnitude of cross-polar cap potential across the 3-hour duration of superposed epoch analysis (Section 3.4: Figure 9 (f)).

Table 6. Summary of the key differences in IMF By and IMF Bz trends observed during STEVE and non-STEVE substorm events

IMF By and IMF Bz	
STEVE events	Non-STEVE substorm events
IMF By has generally low magnitudes for 32 events, and the median value is predominantly negative across the 3-hour duration of superposed epoch analysis (Section 3.3: Figure 6 (g)).	IMF By has generally low magnitudes for 32 events, and the median value is predominantly positive across the 3-hour duration of superposed epoch analysis (Section 3.4: Figure 9 (g)).
The median of IMF Bz gradually decreases from almost zero at 1.5 hours prior to onset to about -3 nT at substorm onset and gradually grows back to -1.5 nT after 1.5 hours post onset (Section 3.3: Figure 6 (h)). Bz temporal variation is less defined.	The median of IMF Bz decreases from almost zero at 1.5 hours prior to onset to about -3 nT at substorm onset at the slow rate at the beginning and more sharply close to onset. It grows back to nearly zero after 1.5 hours post onset. Bz temporal variation is more defined. (Section 3.4: Figure 9 (h)).

Supporting Information for High Latitude Ionospheric Electrodynamics During STEVE and Non-STEVE Substorm Events

V. Svaldi¹, T. Matsuo², L. Kilcommons², and B. Gallardo-Lacourt^{3,4}

¹Mechanical Engineering Department, Colorado School of Mines, Golden, CO, USA

²Ann & H.J Smead Department of Aerospace Engineering Sciences, University of Colorado, Boulder, CO, USA

³Goddard Space Flight Center, National Aeronautics and Space Administration, Greenbelt, MD, USA

⁴Universities of Space Research Association, Columbia, MD, USA

Contents of this file

1. Figures S1 to S5
2. Tables S1

Additional Supporting Information (Files uploaded separately)

1. Captions for Movies S1 to S3

Introduction The supporting information presented in this document primarily seeks to provide supplemental information that was omitted in the main document for the sake of brevity. In this document additional figures displaying the superposed epoch analysis results and reconstructed electrostatic potential maps for all 32 STEVE events centered at the STEVE optical onset time are provided as well as table providing the specific STEVE event dates that had weak dawn cell extension observed in the global ionospheric convection patterns produced by AMGeO. This document also contains superposed epoch analysis results and correlation matrices between principal component coefficients, geomagnetic activity indices, and solar wind parameters for 10 STEVE and 10 non-STEVE substorm events. Movies for events including the STEVE event occurring on March 26, 2008 and on April 5, 2010 and the non-STEVE substorm event occurring on September 14, 2015 are also included.

Text S1: Description of Figure S1-S5 and Table S1 Superposed epoch analysis of time-varying PC coefficients and cross-polar cap potential are shown in the pink colored box-plots in Figure S1 shown for a 3-hour duration centered at the STEVE optical onset. Superposed epoch analysis of AL-index, AU-index, IMF By, and IMF Bz are included to examine the relationship of global modes of ionospheric convection evolution to solar wind drivers and overall substorm evolution indicated by geomagnetic indices. Figure S2 displays reconstructed electrostatic potential distribution maps and median PC coefficients times series at three key time frames at 30 minutes before and after as well as at time of STEVE optical onset. The superposed epoch analysis results for 10 STEVE and 10 non-STEVE substorm events, selected based on SML minimum values, are shown

in Figure S3 and Figure S4, respectively. The related correlation matrices for these events are displayed in Figure S5. Table S1 provides a complete list of four STEVE event dates that did not conform to the majority of the 32 STEVE events investigated in this study with a weak or atypical dawn cell extension observed in AMGeO maps.

Movies showing 5-minute resolution AMGeO maps for a 3-hour duration for the STEVE event occurring on March 26, 2008 and April 5, 2010, and the non-STEVE substorm event occurring on September 14, 2015 are also included.

Movie S1. Movie displaying 5 minute resolution AMGeO electrostatic potential distribution maps generated for case study STEVE event occurring on March 26, 2008 occurring from 6:00 to 9:55 UT. Movie can be viewed at: DOI 10.17605/OSF.IO/F3VUT

Movie S2. Movie displaying 5 minute resolution AMGeO electrostatic potential distribution maps generated for case study non-STEVE substorm event occurring April 5, 2010 from 4:00 UT to 8:25 UT. Movie can be viewed at: DOI 10.17605/OSF.IO/F3VUT

Movie S3. Movie displaying 5 minute resolution AMGeO electrostatic potential distribution maps generated for case study non-STEVE substorm event occurring on September 14, 2015 from 14:00 UT to 17:15 UT. Movie can be viewed at: DOI 10.17605/OSF.IO/F3VUT

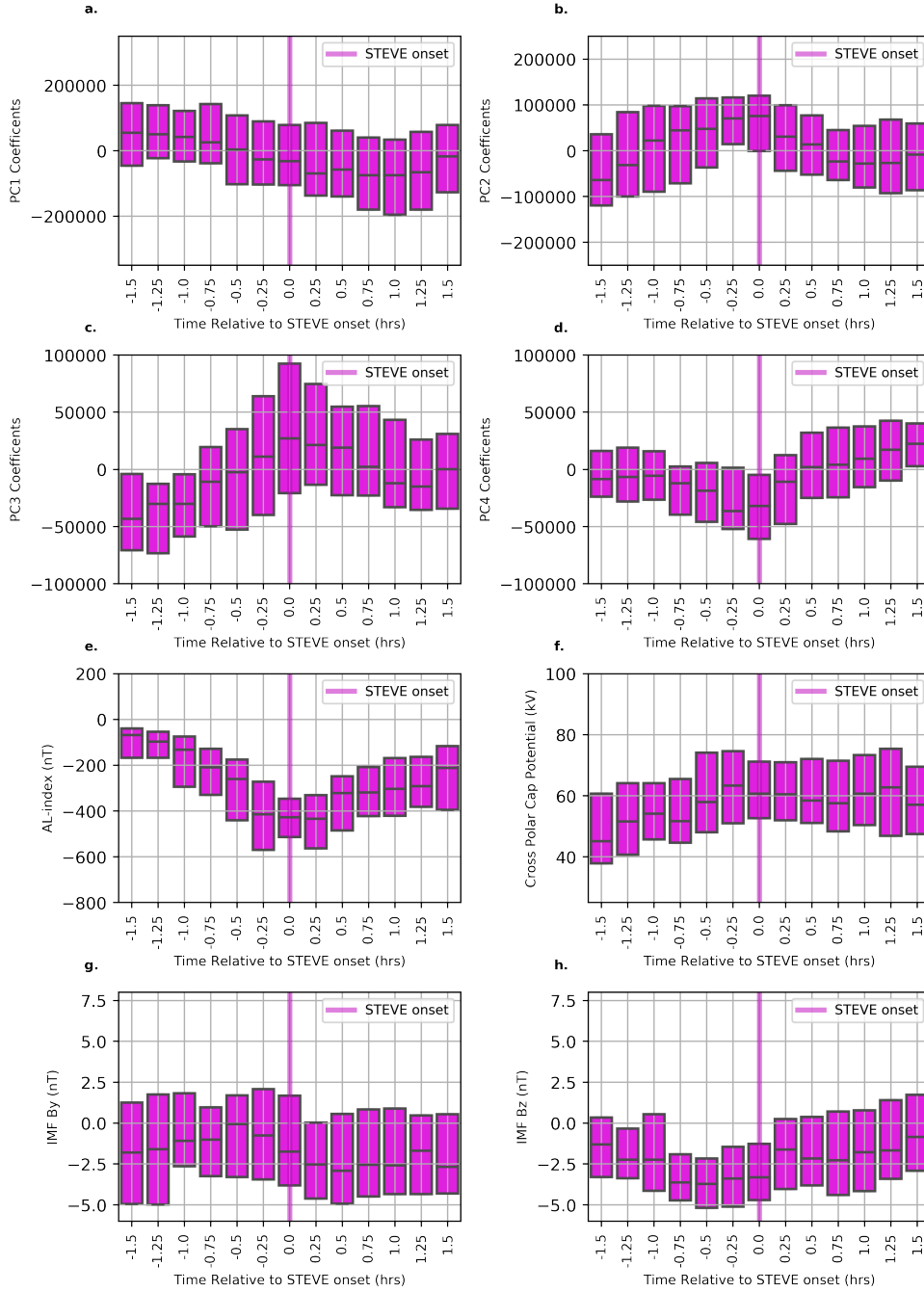


Figure S1. Superposed epoch analysis for all 32 STEVE events for a 3 hour duration centered at STEVE optical onset (1.5 hour prior and 1.5 hour post STEVE optical onset time). Displays the coefficients of the first four PCs, AL-index, AU-index, IMF By/Bz, and cross polar cap potential.

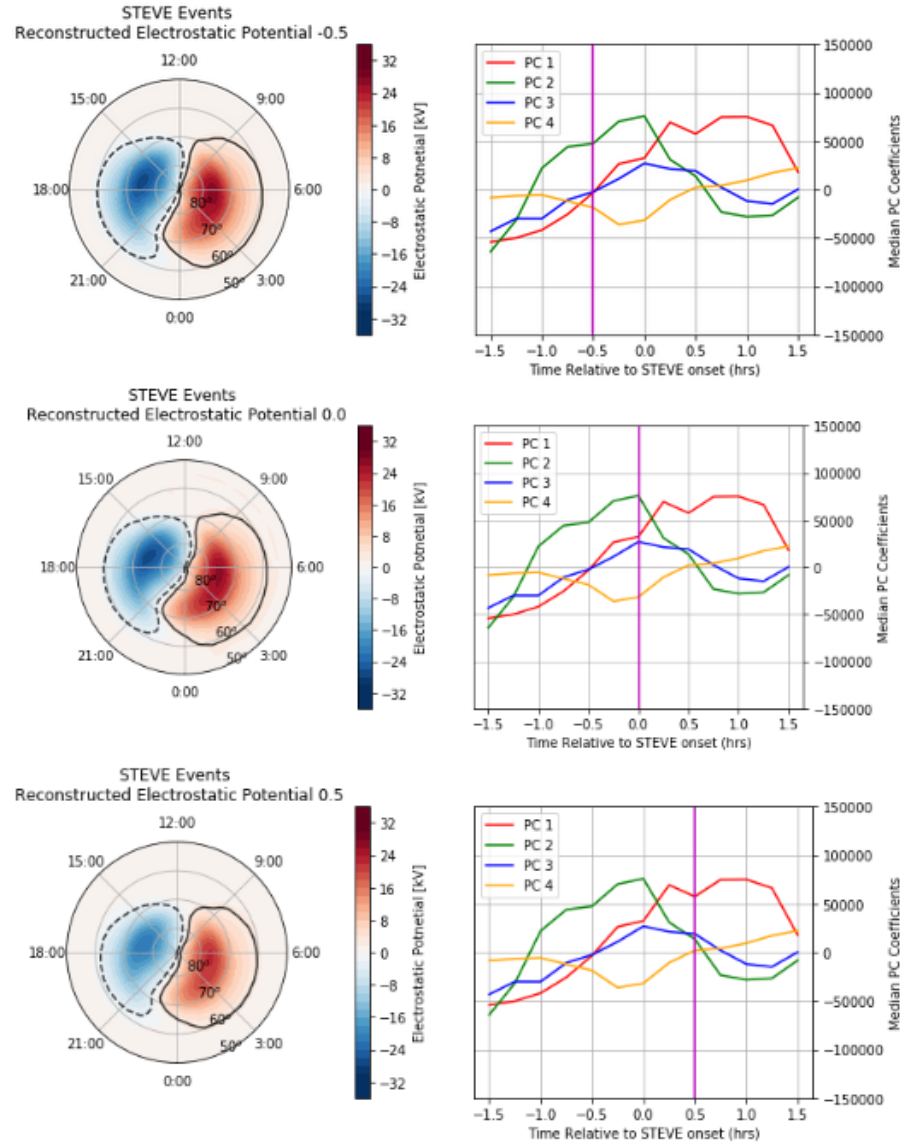


Figure S2. Reconstructed electrostatic potential spatial maps derived from PCA median coefficients for 32 STEVE events and time series of PCA median coefficients for three key times from top to bottom displays maps at 0.5 hour prior to STEVE optical onset, at the STEVE optical onset, 0.5 hour post STEVE optical onset.

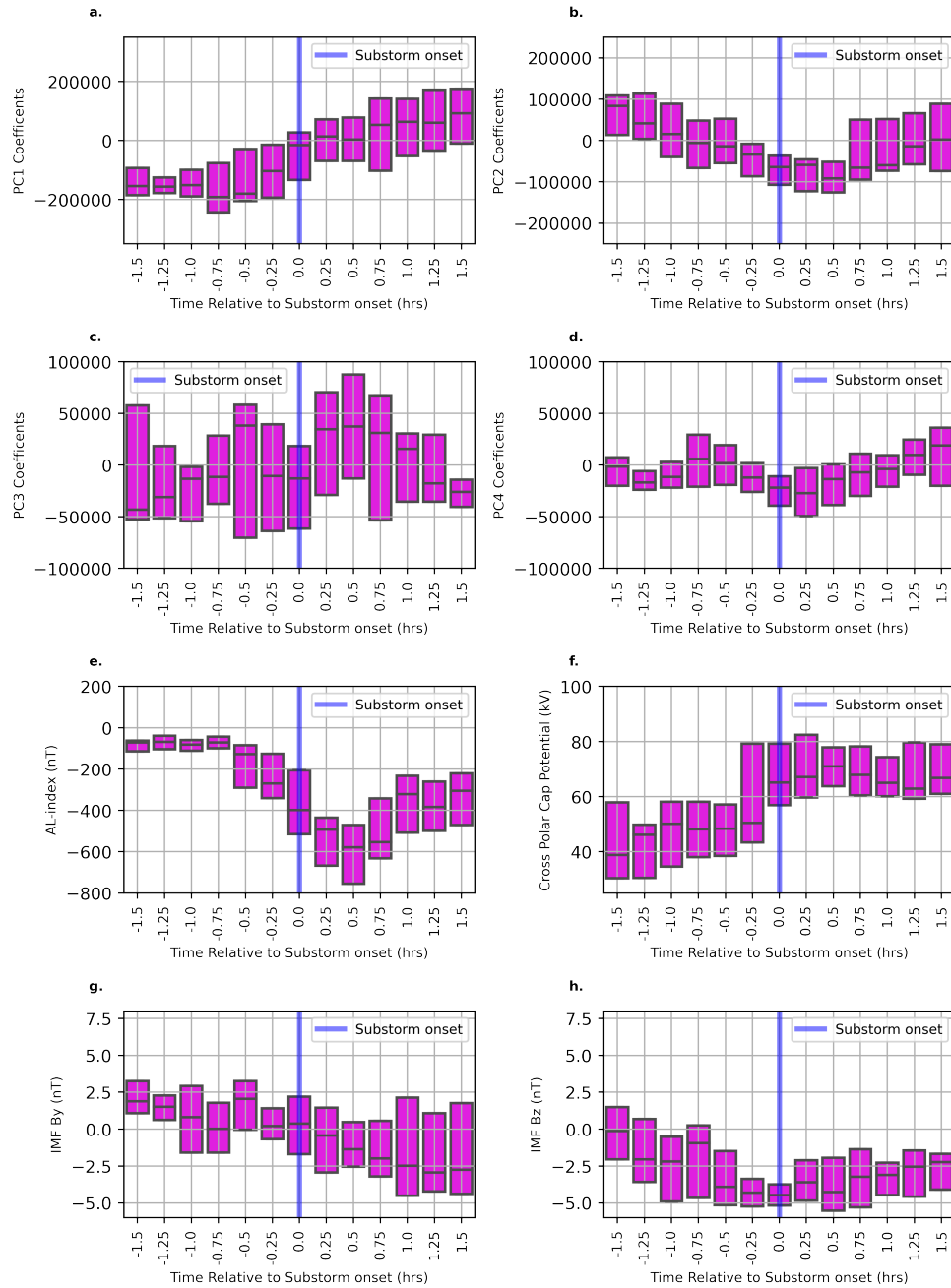


Figure S3. Superposed epoch analysis for 10 STEVE events (events selected based on SML minimum values) for a 3-hour duration centered at substorm onset (1.5 hour prior and 1.5 hour post substorm onset time). Displays the coefficients of the first four PCs, AL-index, AU-index, IMF By/Bz, and cross polar cap potential.

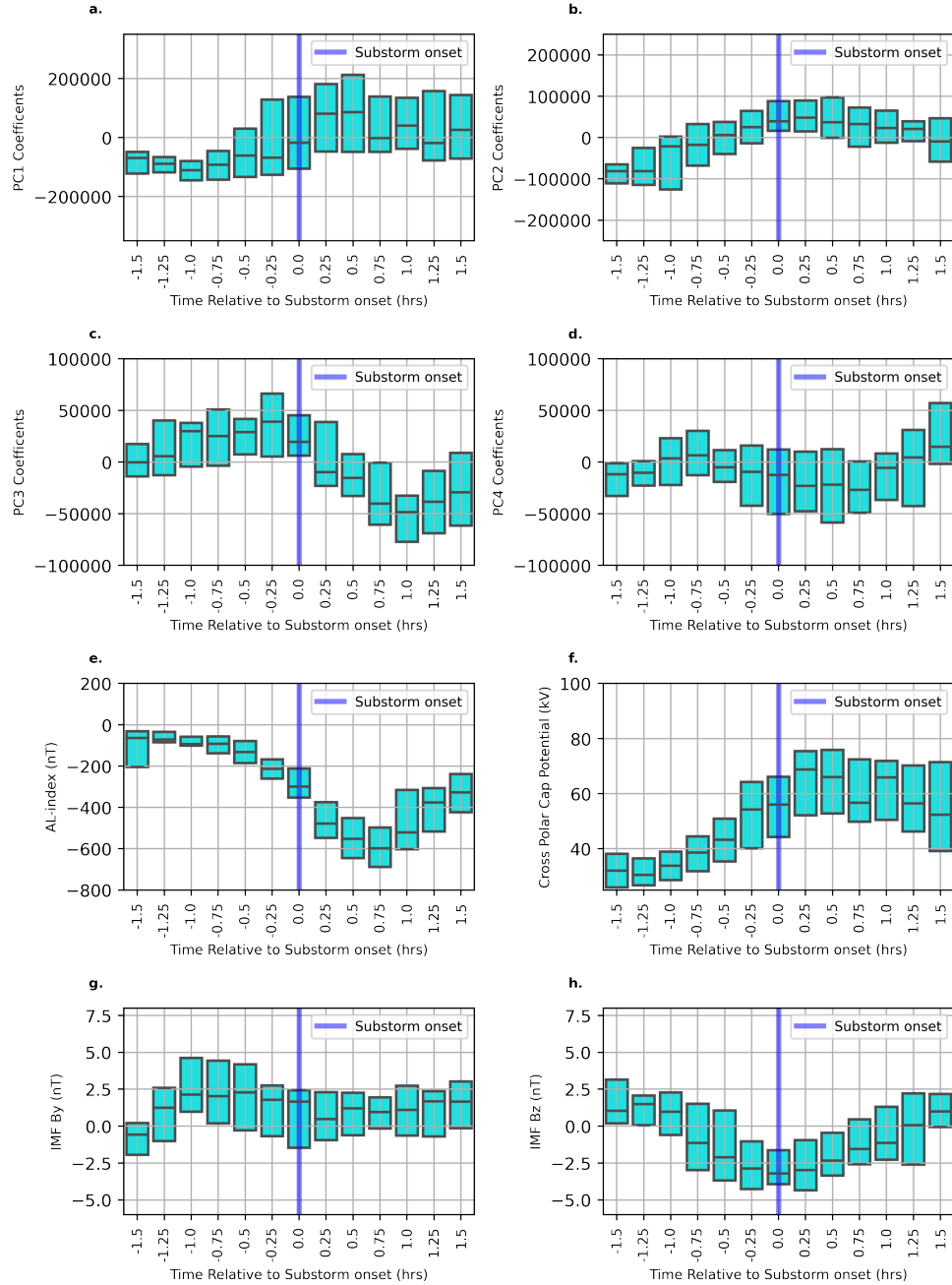


Figure S4. Superposed epoch analysis for 10 non-STEVE substorm events (events selected based on SML minimum values) for a 3-hour duration centered at substorm onset (1.5 hour prior and 1.5 hour post substorm onset time). Displays the coefficients of the first four PCs, AL-index, AU-index, IMF By/Bz, and cross polar cap potential.

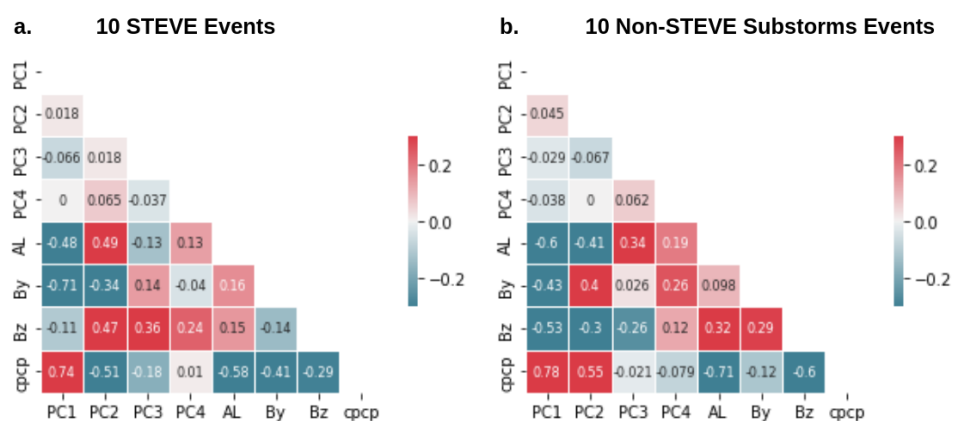


Figure S5. (a) Correlation matrix of PC coefficients, AL-index, AU-index, IMF By, IMF Bz, and cross-polar cap potential for 10 STEVE events. (b) Correlation matrix of PC coefficients, AL-index, AU-index, IMF By, IMF Bz, and cross-polar cap potential for 10 non-STEVE substorm events.

Table S1. List of specific STEVE event dates that had weak or idiosyncratic dawn cell extension observed in the global ionospheric convection patterns produced by AMGeO.

Event	Date	STEVE Onset
1	8-03-2010	5:40
2	6-23-2011	7:15
3	9-13-2013	8:30
4	7-29-2016	5:20